

AD\_\_\_\_\_

Award Number: W81XWH-12-1-0412

TITLE: Proteomic Analysis to Identify Functional Molecules in Drug Resistance  
Caused by E-Cadherin Knockdown in 3D-Cultured Colorectal Cancer Models

PRINCIPAL INVESTIGATOR: Xiaoshan Yue

CONTRACTING ORGANIZATION: University of Notre Dame  
Notre Dame, Indiana 46556

REPORT DATE: September 2013

TYPE OF REPORT: Annual Report

PREPARED FOR: U.S. Army Medical Research and Materiel Command  
Fort Detrick, Maryland 21702-5012

DISTRIBUTION STATEMENT: Approved for Public Release;  
Distribution Unlimited

The views, opinions and/or findings contained in this report are those of the author(s) and should not be construed as an official Department of the Army position, policy or decision unless so designated by other documentation.

REPORT DOCUMENTATION PAGE				Form Approved OMB No. 0704-0188	
Public reporting burden for this collection of information is estimated to average 1 hour per response, including the time for reviewing instructions, searching existing data sources, gathering and maintaining the data needed, and completing and reviewing this collection of information. Send comments regarding this burden estimate or any other aspect of this collection of information, including suggestions for reducing this burden to Department of Defense, Washington Headquarters Services, Directorate for Information Operations and Reports (0704-0188), 1215 Jefferson Davis Highway, Suite 1204, Arlington, VA 22202-4302. Respondents should be aware that notwithstanding any other provision of law, no person shall be subject to any penalty for failing to comply with a collection of information if it does not display a currently valid OMB control number. <b>PLEASE DO NOT RETURN YOUR FORM TO THE ABOVE ADDRESS.</b>					
1. REPORT DATE September 2013		2. REPORT TYPE Annual Report		3. DATES COVERED 1 September 2012 – 31 August 2013	
4. TITLE AND SUBTITLE Proteomic Analysis to Identify Functional Molecules in Drug Resistance Caused by E-Cadherin Knockdown in 3D-Cultured Colorectal Cancer Models				5a. CONTRACT NUMBER W81XWH-12-1-0412	
				5b. GRANT NUMBER W81XWH-12-1-0412	
				5c. PROGRAM ELEMENT NUMBER	
6. AUTHOR(S) Xiaoshan Yue, Amanda B. Hummon  E-Mail: <a href="mailto:xyue@nd.edu">xyue@nd.edu</a> ; <a href="mailto:ahummon@nd.edu">ahummon@nd.edu</a>				5d. PROJECT NUMBER	
				5e. TASK NUMBER	
				5f. WORK UNIT NUMBER	
7. PERFORMING ORGANIZATION NAME(S) AND ADDRESS(ES) University of Notre Dame Du Lac Notre Dame, Indiana 465556				8. PERFORMING ORGANIZATION REPORT NUMBER	
9. SPONSORING / MONITORING AGENCY NAME(S) AND ADDRESS(ES) U.S. Army Medical Research and Materiel Command Fort Detrick, Maryland 21702-5012				10. SPONSOR/MONITOR'S ACRONYM(S)	
				11. SPONSOR/MONITOR'S REPORT NUMBER(S)	
12. DISTRIBUTION / AVAILABILITY STATEMENT Approved for Public Release; Distribution Unlimited					
13. SUPPLEMENTARY NOTES					
14. ABSTRACT During the first year of this research, we put our effort mainly into establishing and optimizing the inducible CDH1 knock down model with 3D culturing system, and evaluating its characteristics and performance. We successfully generated two inducible CDH1-knock-down cell lines (HT29-Green and HT29-Blue) from the parental colorectal cancer cell line HT29, which can express shRNAs targeting to CDH1 under the treatment of doxycyclin. These two cell lines together with one negative control cell line (HT29-Vector) which contains non-specific targeting shRNA are used to establish a model for EMT study in 3D-culture system. We optimized the conditions for initiating 3D structure formation, and found the best conditions for inducing CDH1 knock-down in 3D structures. The optimal conditions are 3000 cells/well seeding density, culturing for less than 10 days, inducing with 2 µg/ml of doxycyclin for 3 days. The CDH1 down regulation was confirmed with RT-PCR analysis, and the cell morphological changes were confirmed with SEM and confocal microscopy observation. The increase of cell migration when down regulating CDH1 was confirmed with Boyden Chamber assay. We also optimized the SILAC methods and developed a new method for phosphoproteomic studies, which was published in Journal of Proteome Research. In conclusion, during the first year, we accomplished most of the work we proposed in our original proposal, and finished the first part of the second year's tasks. The successfully established 3D EMT model will be used for further downstream pathway analysis, and is expected to provide more details on how CDH1 functions during metastatic process.					
15. SUBJECT TERMS CDH1 knock-down, EMT, metastasis, drug resistance					
16. SECURITY CLASSIFICATION OF:			17. LIMITATION OF ABSTRACT	18. NUMBER OF PAGES	19a. NAME OF RESPONSIBLE PERSON
a. REPORT U	b. ABSTRACT U	c. THIS PAGE U			USAMRMC
			UU	40	19b. TELEPHONE NUMBER (include area code)

## Table of Contents

	<u>Page</u>
Introduction.....	4
Body.....	5
Key Research Accomplishments.....	25
Reportable Outcomes.....	25
Conclusion.....	26
References.....	27
Supporting Data.....	28
Appendices.....	30

## INTRODUCTION

Metastasis is one of the biggest problems in cancer therapy. E-cadherin (CDH1) is known to be involved in epithelial-mesenchymal transition (EMT) process, thus playing an important role during the tumor metastatic progression [1-3]. It is reported that losing CDH1 expression in conjunction with EMT might contribute to the development of multidrug resistance (MDR) to chemotherapy [4-6]. Thus, understanding the CDH1 down-regulation mediated EMT and its relationship with MDR will have great benefit for improving chemotherapy efficiency. Most of the present *in vitro* researches analyzing the functions of CDH1 and its involvement in mediating metastasis have been carried out in 2D cultured cell lines. However, it has been reported that cells in 2D-culture systems have different gene expression patterns than *in vivo* cells [7-11]. By comparison, the 3D culture systems provide more accurate molecular pictures of human disease. The establishment of 3D-culture systems will be a better way to mimic the tissue samples and provide us with more information that recapitulates human tissues.

In this research, we aim to establish a 3D model that can simulate the *in vivo* cancer models and can be induced to down regulate its CDH1 expression when stimulated, and thus can be used for simulation of EMT processes. We selected CDH1 as a target for manipulation because its expression is known to cause pronounced chemical and phenotypic changes in epithelial cells. The CDH1 knock down needs to be inducible because expression of CDH1 is essential while forming the 3D structures and the CDH1 will be knocked down after the formation of 3D structures. We hypothesize that by reducing the expression of CDH1 in colorectal cancer cell lines cultured in 3D-structures, the colorectal cancer cells will display EMT characteristics and gain drug-resistance compared to CDH1 (+) colorectal cancer cells. We hypothesize that CDH1 reduction will induce changes in downstream pathways, including proteins in pathways of cell survival (PI3K, GSK3 $\beta$ , EGFR) apoptosis (caspases family proteins, Bcl-2 family proteins), and cell migration (Rho family proteins like Cdc42, Rac1, RhoA, WASP family proteins, and PAR/aPKC complexes). *Our research will be the first to connect EMT to drug resistance in 3D-culture systems.*

During the first year of this research, we put our effort mainly into establishing and optimizing the inducible CDH1 knock down model with 3D culturing system, and evaluating its characteristics and performance. We successfully generated two inducible CDH1-knock-down cell lines (HT29-Green and HT29-Blue) from the parental colorectal cancer cell line HT29, which can express shRNAs targeting to CDH1 under the treatment of doxycyclin. These two cell lines together with one negative control cell line (HT29-Vector) which contains non-specific targeting shRNA are used to establish a model for EMT study in 3D-culture system. The optimized conditions for generating 3D structures

were determined by monitoring the morphologies of 3D structures formed with 12 different seeding densities on 1% agarose coated 96-well plates. The diameters of 3D structures were recorded every day to monitor their growth. Cells were allowed to form 3D structures without doxycyclin treatment, and after 3 days when the 3D structure formed, doxycyclin was added to induce CDH1 knock-down. The expression levels of CDH1 in 3D structures formed with HT29-Vector, HT29-Green and HT29-Blue were compared with real time PCR to confirm the knock down of CDH1. The morphology changes of CDH1-knock-down models were confirmed with scanning electron microscopy (SEM) and the expression of CDH1 was confirmed with confocal microscopy. Boyden chamber assays were carried out to confirm the increase of metastatic ability in CDH1-knock-down 3D structures. The successfully established 3D EMT model will be used for further downstream pathway analysis, and is expected to provide more details on how CDH1 functions during metastatic process.

## **MAIN APPROACHES DURING YEAR ONE**

### **1. Successfully established CDH1-knock-down (CDH1-KD) HT29 cell lines (9/1/2012-12/31/2012).**

We have successfully established CDH-1 knockdown cells lines in HT29s. In our proposal, we had planned to use lipid-based approaches, however, found that lentiviral delivery to be more effective. We had also intended to generate knockdown lines in both HT29 and HCT116; however, only HT29 was amenable to transfection.

As stated in our proposal, we originally expected to have the CDH1-KD cell lines (HT29 and HCT116) established by the time we begin the project. However, unlike the MCF7 cells which we successfully established with FuGENE lipid-based transfection strategy, the HT29 and HCT116 cells showed very low transfection efficiency. After struggling for several months with the FuGENE and lipofectamine 2000 transfection with no success, we changed our strategy and start over with the cell line establishment when the whole project began. Since the lipid-based strategy didn't work, we decided to use the lentiviral system to pack the vectors and infect the cell lines with the lentiviral particles to generate the inducible CDH1-KD cell lines.

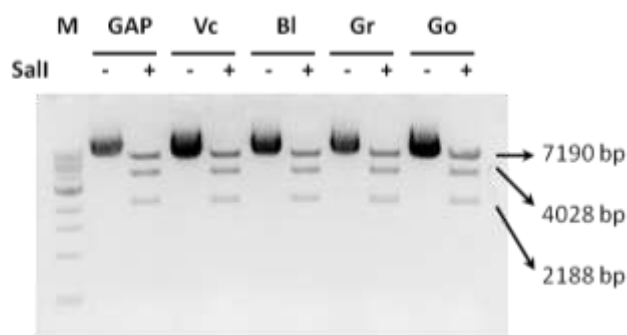
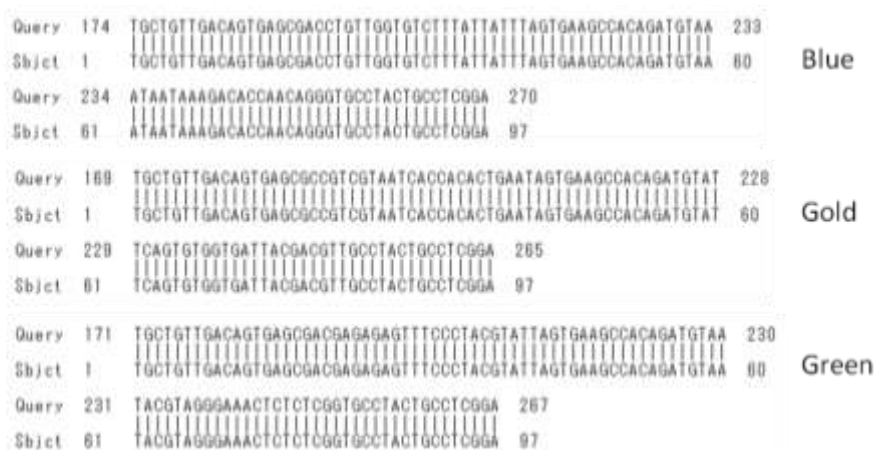
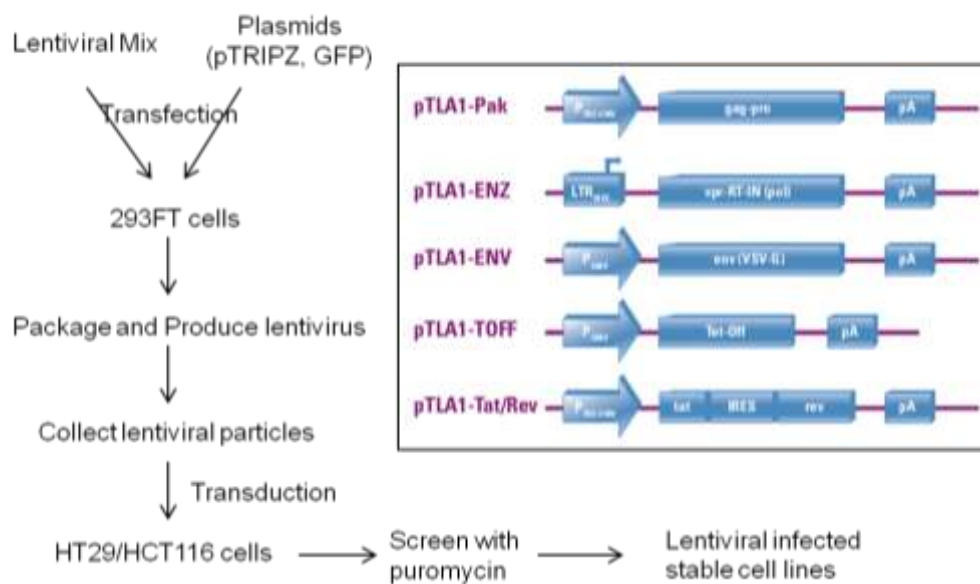
As stated in our proposal, 5 types of plasmids were generated, including three CDH1-KD vectors, which we refer to as Gold, Blue, and Green, which contain shRNA sequences that target different part of CDH1 (Table 1), one negative control vector described as Vector which contains an shRNA sequences with no specific targets, and one positive control vector that targets GAPDH. For the quality control of the 5 types of

pTRIPZ vectors, they were treated with restriction enzyme SalI. All 5 purified vectors showed 1 intact band without SalI treatment and 3 bands with SalI treatment (Figure 1A), indicating that the quality of the vectors are good. To further confirm the precise shRNA sequence, all 5 vectors were sequenced and the sequencing results were compared with the theoretical shRNA sequences. The alignment results showed that all the shRNAs that target CDH1 were 100% precise (Figure 1B).

**Table 1.**shRNA sequences for CDH1 knock down.

Commercial #	Artificial Name	Hairpin sequences	Targets
V2THS_14834	Blue	TGCTGTTGACAGTGAGCG <b>ACCTGTTGGTCTTTATTATT</b> <b>AGTGAAGCC</b> <b>ACAGATGTA</b> AATAATAAGACACCAACAGGGTGCCTACTGCCTCGGA	726-744
V2THS_14838	Gold	TGCTGTTGACAGTGAGCG <b>CGTCGTAATCACCACACTGA</b> <b>AGTGAAGCC</b> <b>CACAGATGTA</b> <b>TTCAGTGTGGTGATTACGACG</b> TGCCTACTGCCTCGGA	1295-1313
V2THS_243170	Green	TGCTGTTGACAGTGAGCGACGAGAGAGTTTCCCTACGTAT <b>AGTGAAGCC</b> <b>ACAGATGTA</b> <b>ATACGTAGGGAACTCTCTCGG</b> TGCCTACTGCCTCGGA	1128-1146
Red: shRNA sense; Blue: shRNA anti-sense; Green: mir-30 loop			

The lentiviral infection procedure is shown in Figure 1C. 293FT cells were first transfected with 5 pieces of lentiviral particles together with different types of pTRIPZ vectors. The vectors are packed into the lentiviral particles. A green fluorescence expression plasmid was also co-transfected into 293FT cells to evaluating the transfection efficiency based on the green fluorescence. Because it doesn't contain the lentiviral packing sequence, it will not affect the packing process of our aim vectors. The transfection efficiency of 293FT is shown in Figure 1D, evaluated based on expression of green fluorescence. The data in this figure shows that the lentiviral particles and plasmids were transfected into 293FT cells with very high efficiency.

**A****B****C**

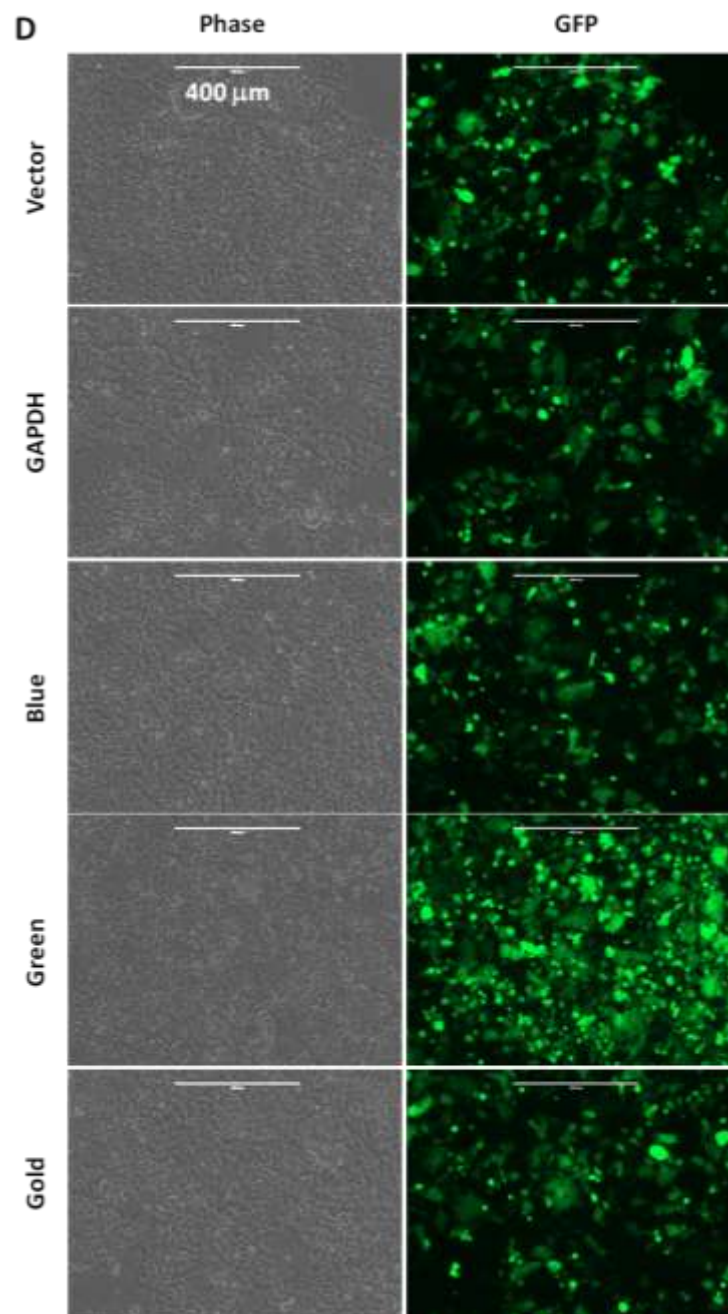


**Figure 1.** Confirmation of vector purification and lenti-virus packaging. (A) Purified vectors were digested with SalI showing 3 bands. (B) Blast of shRNA sequences incorporated in the purified vectors against the theoretical sequences. All shRNA sequences showed 100% alignment with the theoretical sequences. (C) Brief procedure for lenti-virus packaging. (D) Lenti-virus packaging in 293 FT cells. A vector expressing GFP were co-transfected into the 293FT cells to indicate the transfection efficiency.



After successfully generating lentiviral particles containing the 5 different types of pTRIPZ vectors, the lentiviral particles were purified and used for infecting two colorectal cancer cell lines (HT29 and HCT116). For each cell line and each type of pTRIPZ vector, we infected the cells with two different batches of lentiviral particles, and for the first batch of lentiviral particles, 3 different titer amounts (1 ml, 0.5 ml, and 0.25 ml) were tested in parallel (Table 2). In summary, 10 different cell lines were generated under 40 different conditions and screened with puromycin for at least 2 weeks to establish stable pTRIPZ containing cells.

**Table 2.** Lentiviral infection conditions.

	HT29				HCT116			
	Virus-Batch 1			Batch 2	Virus-Batch 1			Batch 2
	Titer1	Titer2	Titer3	Titer1	Titer1	Titer2	Titer3	Titer1
Vector	1	1	1	1	1	1	1	1
GAPDH	1	1	1	1	1	1	1	1
Green	1	1	1	1	1	1	1	1
Blue	1	1	1	1	1	1	1	1
Gold	1	1	1	1	1	1	1	1
Total: 40 infection conditions								

Doxycyclin was then added to these established cell lines to induce the expression of TurboRFP together with shRNAs. Red fluorescence was observed with each cell line. For modified HT29 cell lines, red fluorescence was observed in most of the infection conditions (Figure 2). In addition to expressing strong fluorescence intensity, the “Blue (Bl)” and “Green (Gr)” CDH-1 knockdown cells showed altered, rounded morphology (Figure 2, Rows 3 & 4). On the contrary, for modified HCT116 cell lines, weak red fluorescence was only observed in several conditions and the fluorescence decreased with each passage (data not shown).

The down-regulation of CDH1 was confirmed with RT-PCR. For HT29 cell lines, HT29-Green and HT29-Blue showed the best CDH1 knock-down, while GAPDH expression was unchanged (Figure 3A). While for HCT116 cell lines, HCT116-Green and HCT116-Blue showed only mild down-regulation of CDH1, and HCT116-Gold showed no CDH1 knock-down effects (Figure 3B). These results are in accordance with the TurboRFP observation. Especially for the HT29-Green and HT29-Blue cells, after inducing CDH1-KD shRNA expression, cells showed an altered, rounded morphology, compared with HT29-Vector, HT29-GAPDH and HT29-Gold cells (Figure 2). In addition, different virus titer seemed to have no obvious effect on CDH1 knock-down

efficiency (Figure 3A. Green and Blue). As a result of these observations, only HT29-Green and HT29-Blue with virus-1 were chosen for later experiments and HT29-Vector was used as negative control for CDH1-KD.

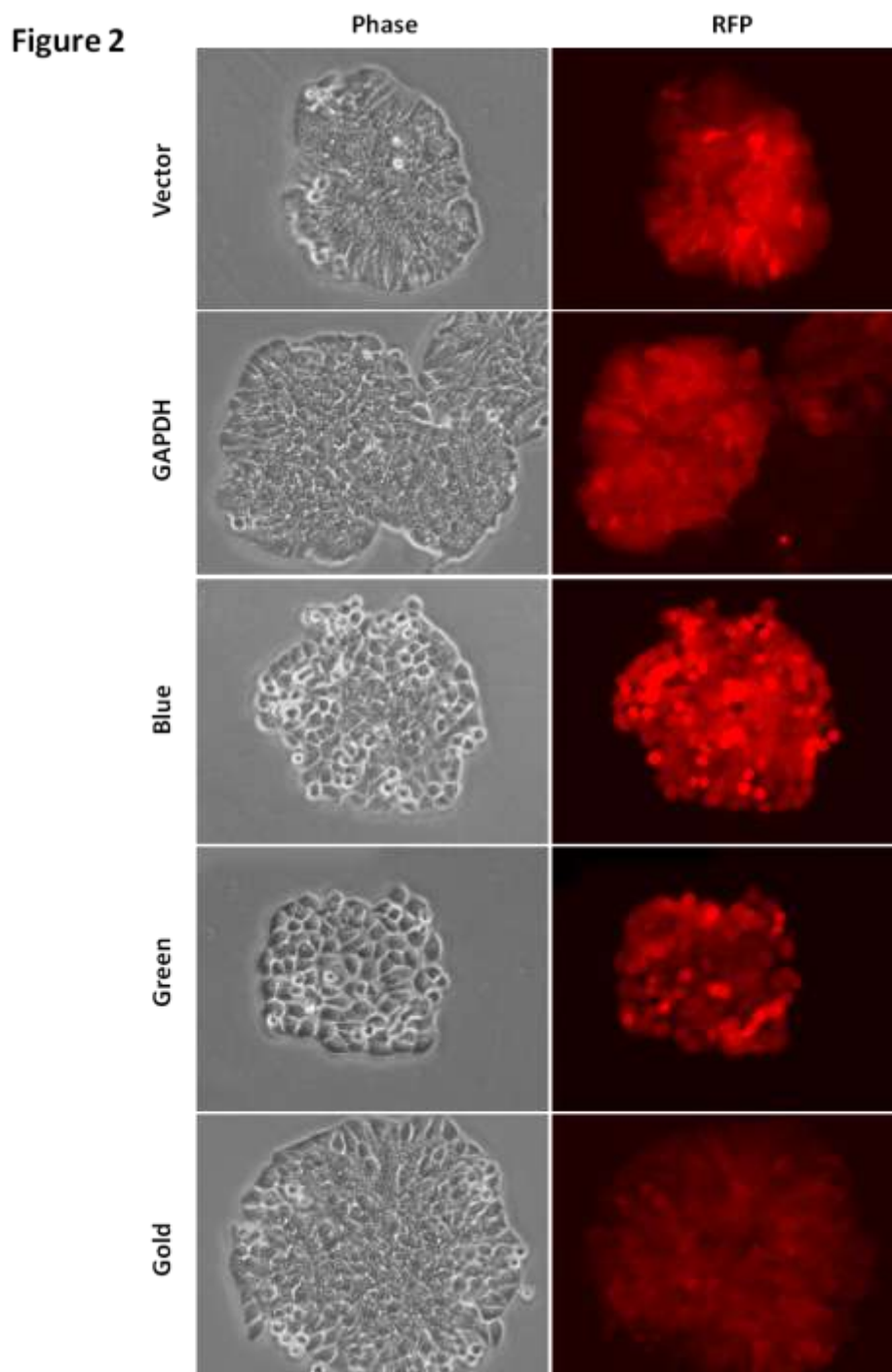
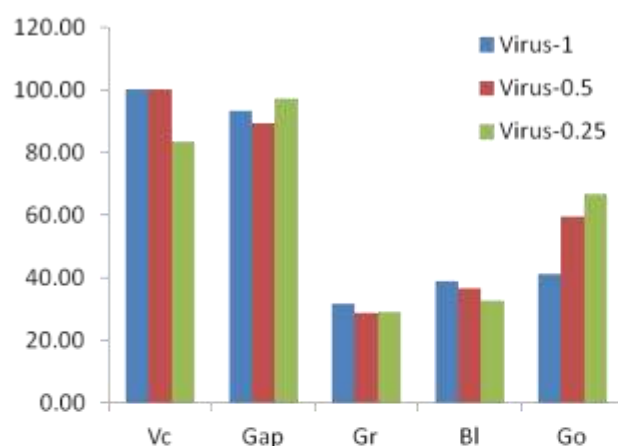


**Figure 2.** Morphology of HT29 cells after infection with five types of lentiviral particles and screening with puromycin for 14 days. The cells that survived in puromycin screening were treated as shRNA/TurboRFP expressing cells and

induced to express shRNA/TurboRFP by adding 1 $\mu$ g/ml doxycyclin. Red fluorescence indicates the expression of Turbo RFP, which also indicates the expression of shRNAs. Morphology changes can be observed in CDH1-KD shRNA expression cells.

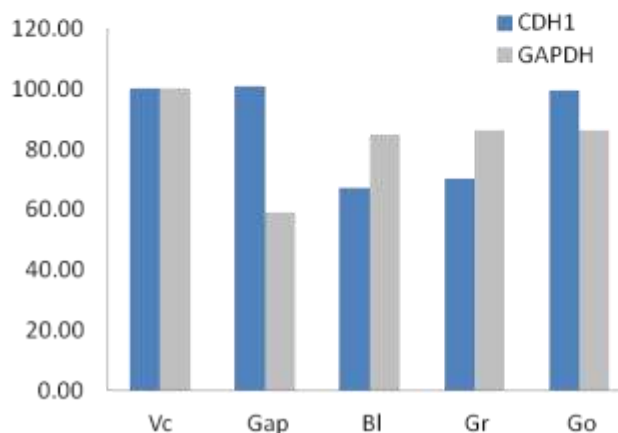
**Figure 3**

**A**



Sample	Remaining RNA
Vc1-D4	100.00
Vc0.5-D4	100.00
Vc0.25-D4	83.46
Gap1-D4	93.18
Gap0.5-D4	89.46
Gap0.25-D4	97.20
Gr1-D4	31.54
Gr0.5-D4	28.83
Gr0.25-D4	28.94
Bl1-D4	38.86
Bl0.5-D4	36.53
Bl0.25-D4	32.53
Go1-D4	41.25
Go0.5-D4	59.53
Go0.25-D4	66.88

**B**



Sample	Remaining RNA
CDH1	
Vc1-D3	100.00
Gap1-D3	100.77
Bl1-D3	67.05
Gr1-D3	70.35
Go1-D3	99.57
GAPDH	
Vc1-D3	100.00
Gap1-D3	58.87
Bl1-D3	85.00
Gr1-D3	86.27
Go1-D3	86.15

**Figure 3.** Confirmation of knock-down of CDH1 RNA expression in 2D culturing system with RT-PCR. (A) HT29 cell lines were analyzed with different virus amounts containing different shRNAs. (B) HCT116 cell lines were analyzed for expression of CDH1 and GAPDH.

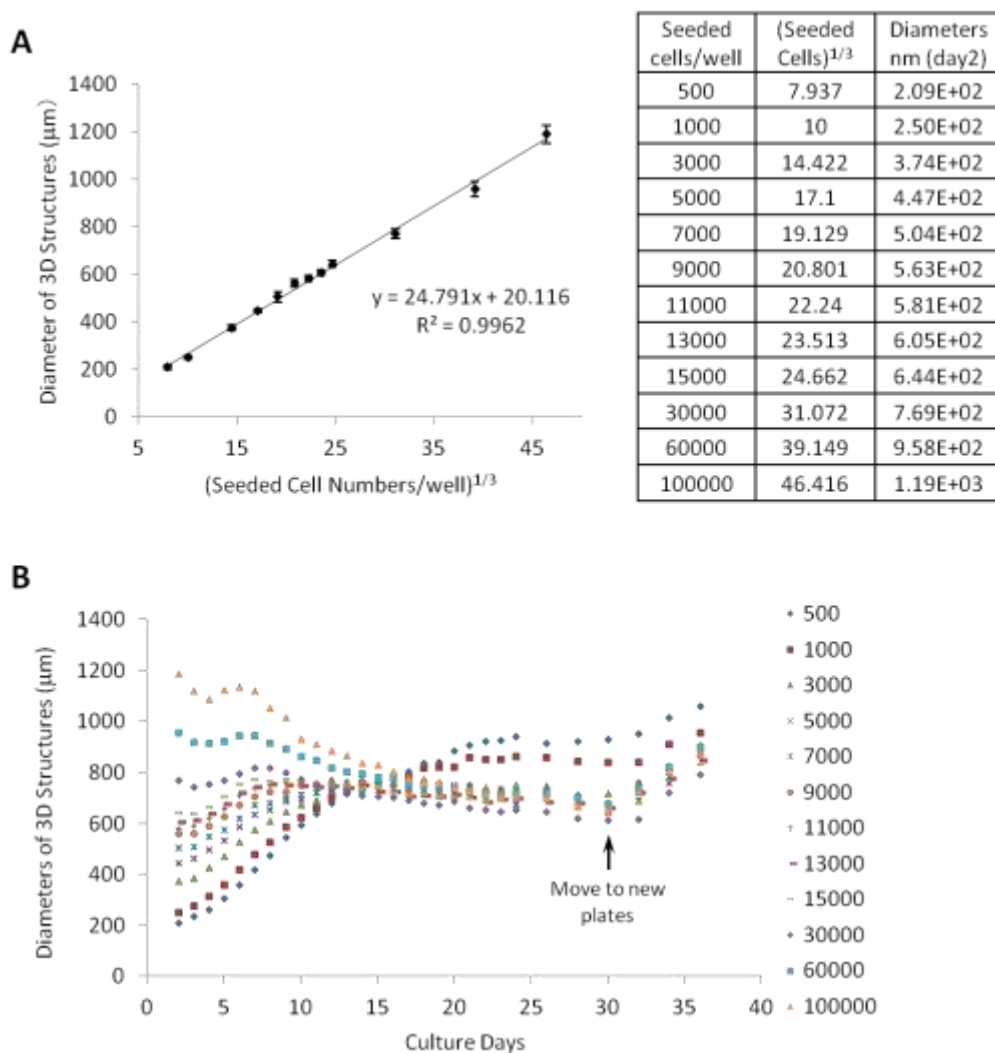
## **2. (Task 1a) Optimize culture conditions for forming 3D structures. (12/1/2013-2/28/2013)**

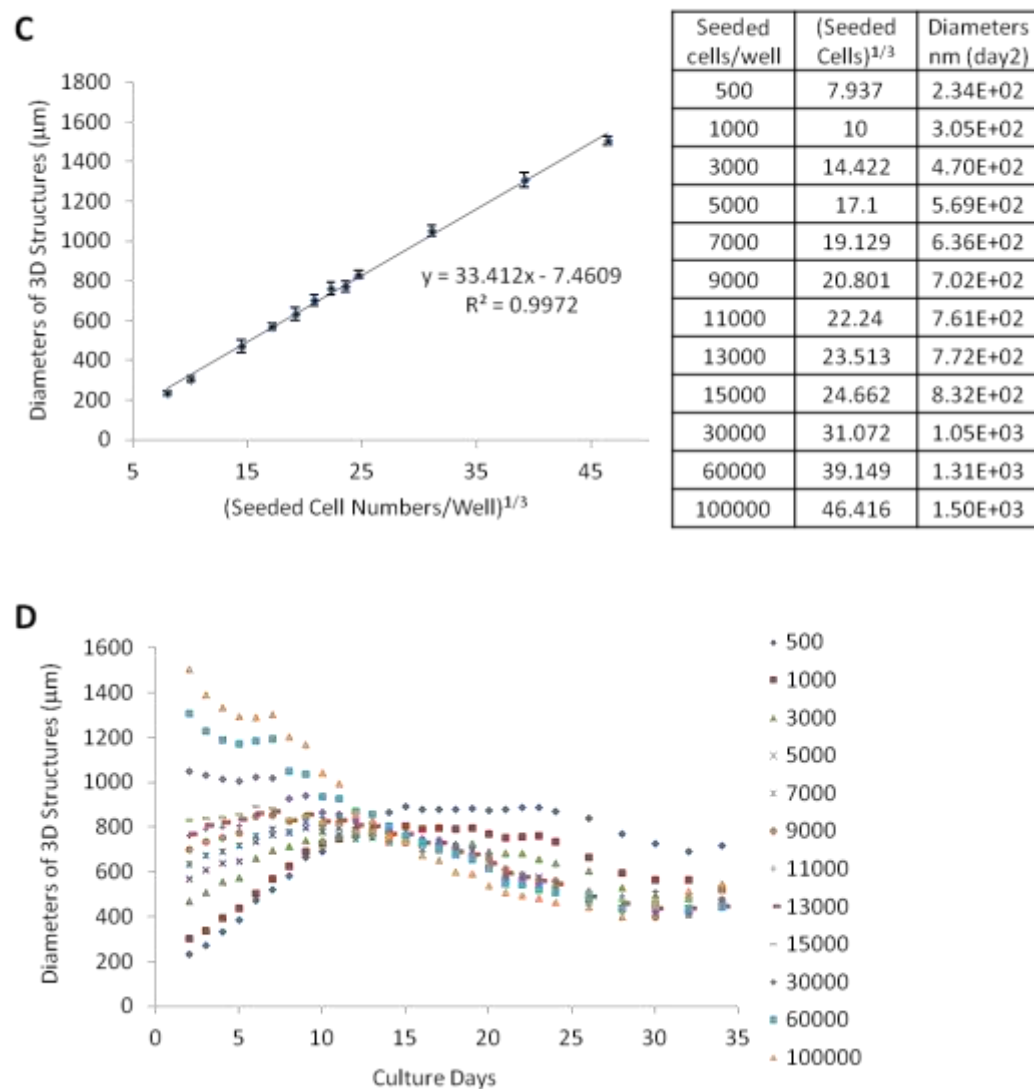
Non-transfected HT29 and HCT116 cells were first used for optimization of conditions to form 3D structures. For each cell line, 12 different seeding densities were tested, as shown in Figure 4A and Figure 4C. After seeding onto the agarose coated 96-well plates, cells will aggregate at the round bottom of the wells and 3D cell structures can be observed from day 2. Because on Day 2 most of the cells haven't proliferated yet and the proliferation of seeded cells can be neglected, the volume of the 3D structures can be approximately treated as similar to the seeded cell numbers. We measured the diameter of the 3D structures on Day 2 and both HT29 and HCT116 cell lines showed good agreement between the measured diameters and the cube roots of correspondent seeding densities (Figure 4A and 4C), with  $R^2$  of 0.996 for HT29 cells and 0.997 for HCT116 cells. After the initiation of 3D structure formation, cells within the 3D structures began to proliferate and the 3D structure increased in size. To monitor their proliferation, we acquired optical images of the 3D structures every 24 hours from day 2 to day 24, and every 48 hours from day 24 to day 36 for HT29 cells, and to day 34 for HCT116 cells. With each seeding density, we observed 10 different wells to account for biological variation and minimize recording errors. We generated 3,480 pictures for the HT29 cell cultures and 3,360 pictures for HCT116 cell cultures. The 3D structure diameters were measured for each picture and the results were analyzed with MATLAB. The figures of diameters of 3D structures verses the number of days in culture were generated as shown in Figure 4B and 4D. The numerical diameters and their standard deviations are reported in Table 3 (HT29 cells) and Table 4 (HCT116 cells). As shown in Figure 4B, for HT29 cells, when seeding densities are lower than 15,000 cells/well, cells grow for the first several days with different growth rates. However, for those with seeding densities higher than 15,000 cells/well, the formed 3D structures do not increase in diameter with culturing time. All the 3D structures with different seeding densities become similar size at day 15. Between days 25 and 30, the size of the cultures remain constant for many seeding densities. However, after transfer to a new agarose plate, they began to grow again (Figure 4B arrow).

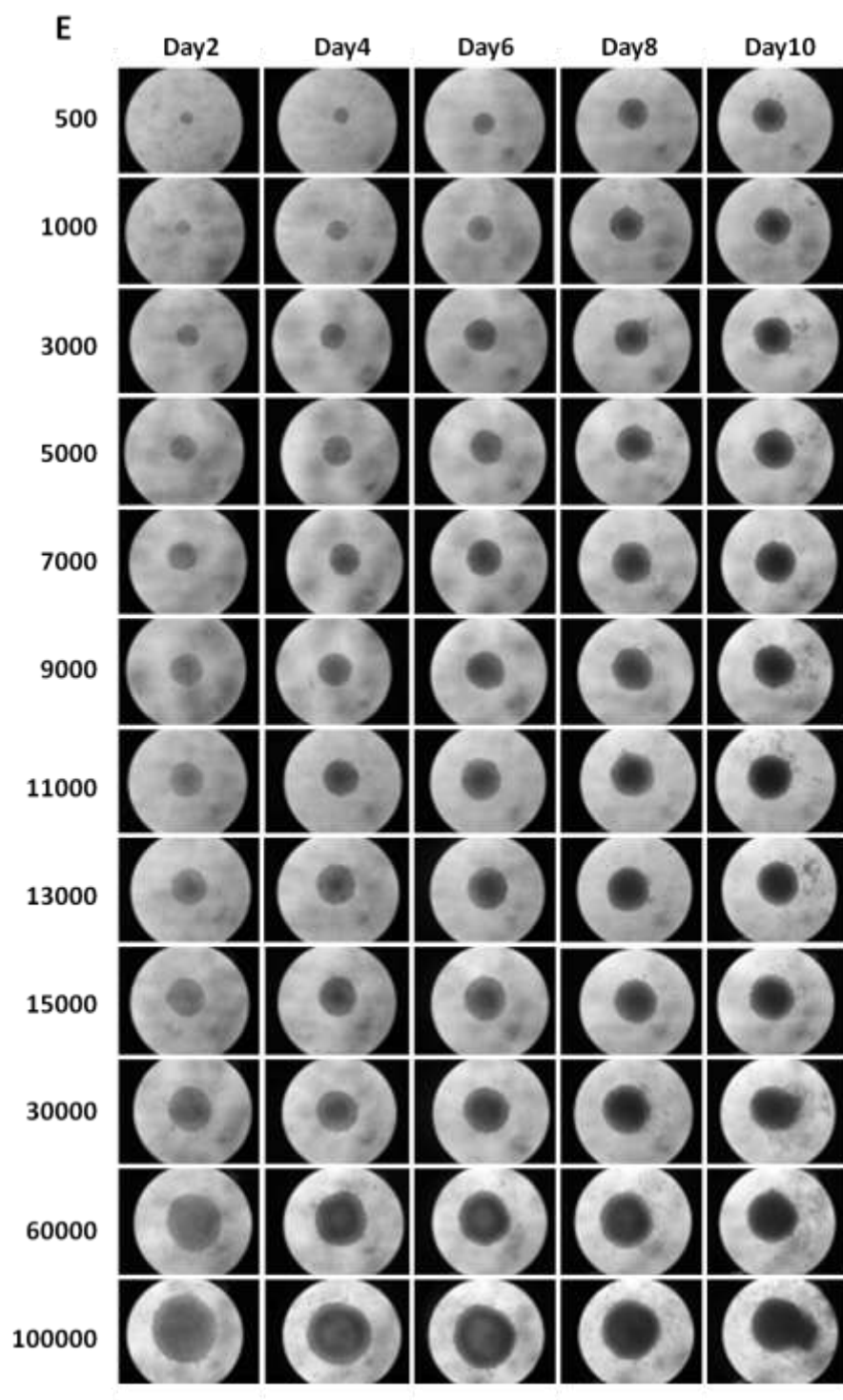
As shown in Figure 4D, for HCT116 cells, the 3D structures showed similar characteristics as HT29 cells, and all 3D structures with different seeding densities showed similar size at day 13. Then the 3D structures stopped growing and those with higher seeding densities began to collapse (Figure 4D). The morphologies of the 3D structures formed with different seeding densities are shown in Figure 4E for HT29 cells and Figure 4F for HCT116 cells. For the higher seeding densities, the 3D structures appeared to be less viable as early as day 10. To confirm that the HT29-Green, HT29-

Blue and HT29-Vector cells have similar proliferation properties as the non-transfected HT29 cells, the same density of these cells were seeded and monitored every day. Their morphologies at day 7 were shown in Figure 5. They did not show much difference during the proliferation process. To keep the cells viable and proliferating during experiments, we chose the seeding density of 3000 cells/well and kept the overall culturing time within 15 days. The one exception is for the SEM observation, when for manipulation convenience, we used the seeding density of 7000-9000 cells/well.

**Figure 4**



**Figure 4**



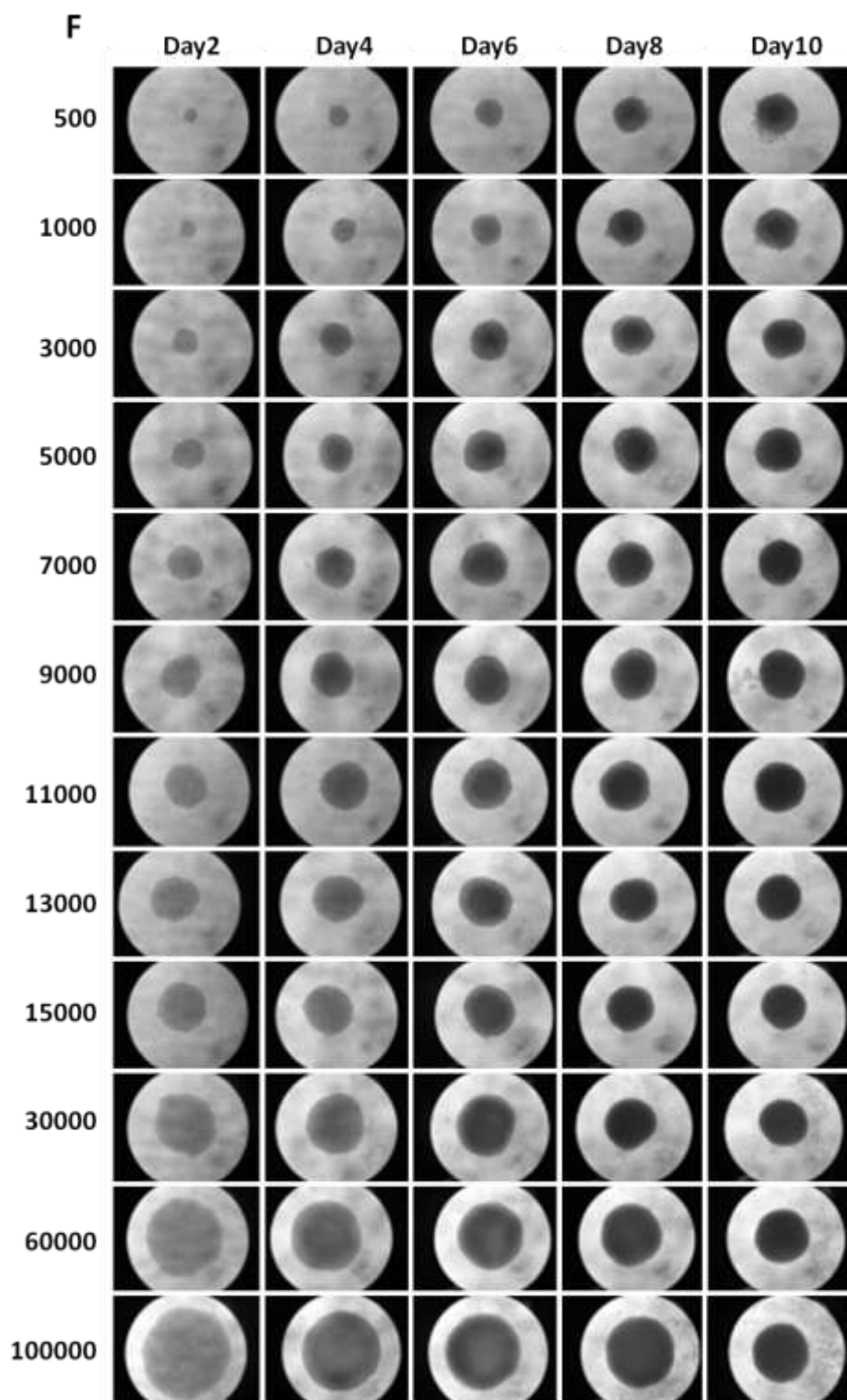


**Fig 4.** Optimization of the conditions to form 3D structures. (A) Relationship of seeding densities and diameters of 3D structures of HT29 cells. (B) Growing curve of HT29 cells seeded with different seeding densities. The growth of 3D structures is evaluated by their diameters. (C) Relationship of seeding densities and diameters



of formed 3D structures of HCT116 cells. (D) Growing curve of HCT116 cells seeded with different seeding densities. The growth of 3D structures is evaluated by their diameters. (E, F) Pictures of 3D structures on different culturing days with different seeding densities. (E) HT29 cells, and (F) HCT116 cells.

**Figure 5**

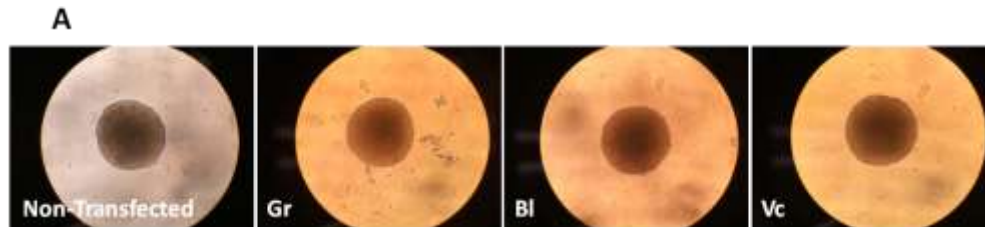


**Fig 5.** Morphology of 3D structures formed by HT29-Vector, HT29-Green, HT29-Blue and non-transfected HT29 cells at seeding density of 8000 cells/well on day 7.

### **3. (Task 1b) Optimize conditions for inducing CDH1 knock-down in 3D system. (3/1/2013-5/31/2013)**

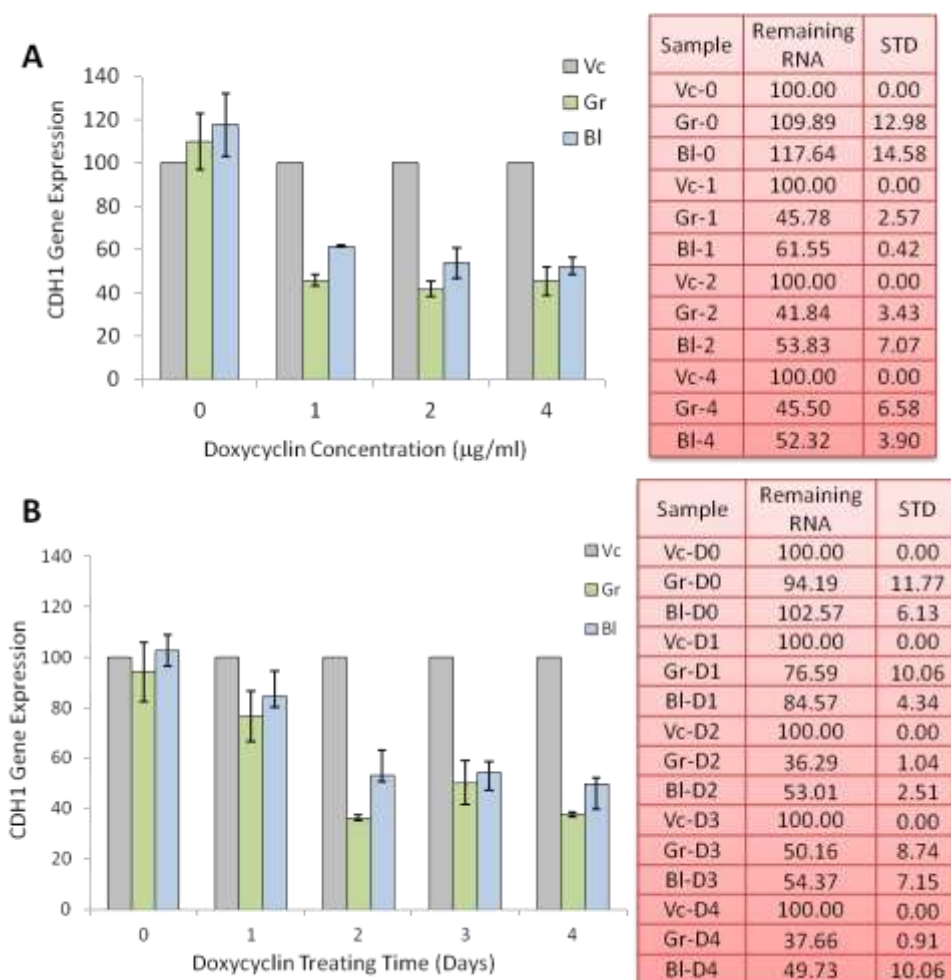
In Figure 3, we showed the CDH1 knock-down in 2D culture system. Since the 3D culture system is different from the 2D culture system, we further optimized the conditions for inducing CDH1 knock-down in the 3D culture system. The amounts of doxycyclin for inducing CDH1-KD shRNA expression were first optimized. Six different doxycyclin concentrations were evaluated (with final concentrations of 1  $\mu\text{g/ml}$ , 2  $\mu\text{g/ml}$ , 4  $\mu\text{g/ml}$ , 8  $\mu\text{g/ml}$ , and 12  $\mu\text{g/ml}$ ). The 3D structures without adding doxycyclin (0  $\mu\text{g/ml}$ ) were used as a control group. After 4 days of treatment with doxycyclin, the 3D structures in groups with high doxycyclin concentrations (8  $\mu\text{g/ml}$  and 12  $\mu\text{g/ml}$ ) began to disintegrate so that they were discarded without an evaluation by RT-PCR (data not shown). The toxicity of doxycycline at high concentrations might be the reason for the disintegration. As a result, only 3D structures treated with doxycyclin concentrations less than or equal to 4  $\mu\text{g/ml}$  were further analyzed for CDH1 expression with RT-PCR. The CDH1 expression in HT29-Green and HT29-Blue were normalized to that in HT29-Vector treated with the correspondent doxycyclin concentrations (Figure 6A). The results indicated that treatment with 1  $\mu\text{g/ml}$  of doxycyclin is sufficient to induce CDH1 down-regulation at RNA level, and further increasing the doxycyclin concentration did not show much improvement on CDH1 knock-down efficiency (Figure 6A).

For the next step, the doxycyclin treatment time was also optimized. 3D structures treated with 2  $\mu\text{g/ml}$  doxycyclin for 0 day, 1 day, 2 days, 3 days, and 4 days were

collected separately and checked for their CDH1 mRNA expression (Figure 6B). The CDH1 expression in HT29-Green and HT29-Blue were normalized to that in HT29-Vector treated with doxycyclin for the correspondent times. The results indicated that by 2 days of treatment with 2  $\mu\text{g/ml}$  of doxycyclin, the CDH1 expressions are down-regulated for more than 50% at RNA level, and the decrease of CDH1 expression did not show many changes by further increasing the doxycyclin treatment time (Figure 6B).

With the above optimization, considering the possible delay from RNA expression to protein expression, 2  $\mu\text{g/ml}$  of doxycyclin and treatment for 3 days were selected for later experiments.

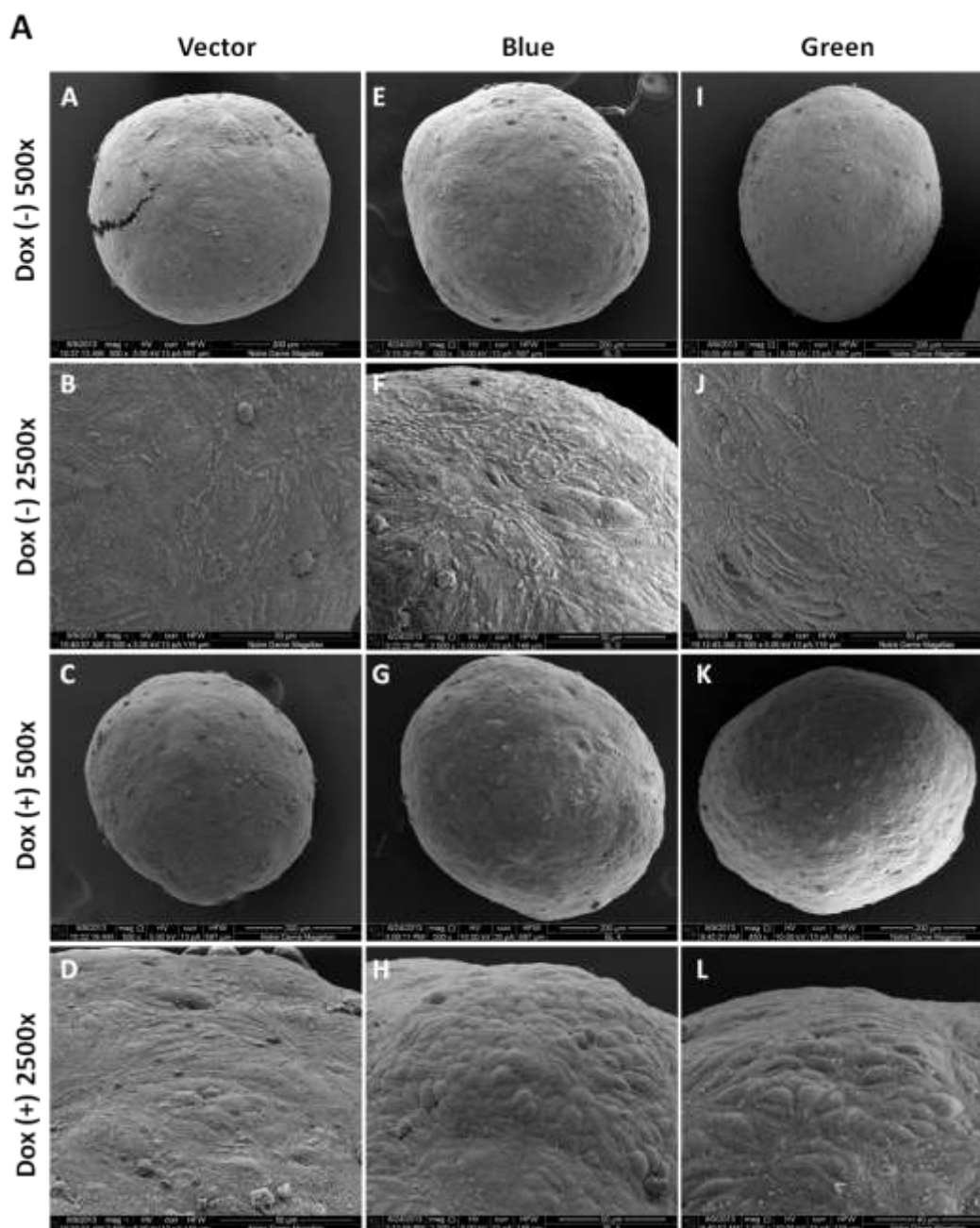
**Figure 6**



**Figure 6.** Optimization of doxycyclin treatment conditions for inducing CDH1 down regulation in 3D culturing system. (A) RT-PCR results for optimization of doxycyclin treatment dose. (B) RT-PCR results for optimization of doxycyclin treatment time.

**4. (Task 1c) Confirm morphological cell response to reduced CDH1 expression.**  
**(6/1/2013-8/31/2013)**

Morphological changes induced by CDH1 down-regulation was first confirmed with scan electron microscope (SEM). HT29-Vector, HT29-Blue and HT29-Green cells were seeded at the density of 8000 cells/well and cultured for 10 days followed with 3 days treatment with 2 µg/ml doxycyclin. This experimental condition was selected because at day 13 with 8000 cells/well seeding density, the 3D structures are big and sturdy enough to be manipulated for SEM sample preparation. Without doxycyclin treatment, HT29-Blue and HT29-Green 3D structures showed no morphological differences compared with HT29-Vector 3D structures (Figure 7A, B, E, F, I and J). Cells on the surface of the 3D structures were smoothly integrated with each other and individual cells are not clearly defined. However, with doxycyclin treatment for 3 days, HT29-Blue and HT29-Green 3D structures showed very clear morphological changes to the surface cells (Figure 7G, H, L and K), having less integration with each other and clearer individual cell structures. In contrast, the HT29-Vector 3D structures are not visibly altered with doxycyclin treatment (Figure 7C and D). These results suggest that CDH1 knock-down with shRNA induced by doxycyclin treatment will cause reduced integration of the surface cells, potentially leading to migration.

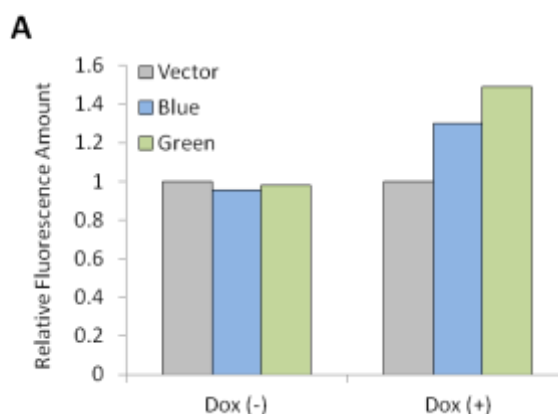
**Figure 7**

**Figure 7.** Surface morphology of HT29-Vector, HT29-Blue and HT29-Green 3D structures were confirmed with SEM. The intact spheroid structures are shown in Rows 1 & 3, while the surface of the spheroids are shown in Rows 2 & 4. Note the changes in the surface cells that occur for the Blue and Green cell lines with the additional of Doxycycline (Row 4, H and J).

A Boyden chamber assay was then performed to quantitatively evaluate the migratory of different 3D structures with or without doxycyclin treatment. The number of cells migrated from the upper chamber to the lower chamber were evaluated by the fluorescence intensity. All data were normalized to HT29-Vector 3D structures with corresponding doxycyclin treatment conditions. The results showed that with doxycyclin treatment, more migrating cells were detected in HT29-Blue and HT29-Green 3D structures (Figure 8A). However, because the 3D structures easily stick on the upper chamber surface and are difficult to remove, only one of the three replicates attempted succeeded. We are currently working to replicate this experiment as well as searching for other methods that are easier to perform.

Immunostaining of CDH1 and observation with confocal microscope was originally proposed to confirm the expression of CDH1 with or without doxycyclin treatment, and cells at inner part of 3D structures were expected to be observable via confocal microscopy. However, when we tried the experiment with 3D cultures of HT29-Green, as shown in Figure 8B, with increase of frame numbers (indicating the distance from the bottom of 3D structures, with the lowest surface which contact with bottom cover glass referred to as Frame 1), the staining signal of the inner part became weaker and weaker. We consider the possible reasons might be as follows: 1) the staining process is not long enough to allow the antibodies and/or DAPI to penetrate into the inner part of the 3D structures (we can only observe up to 2-3 layers of cells from the surface); and 2) the setting of the confocal laser is not powerful enough to give us information of the inner part of the 3D structures. The Notre Dame imaging facility is recently adjusting and optimizing a multiphoton confocal instrument. Once it is available for our use (within the next 2-3 weeks), we will repeat these experiments with the multiphoton settings. With the improved instrument settings, we hope to obtain images throughout the 3D structures.

**Figure 8**



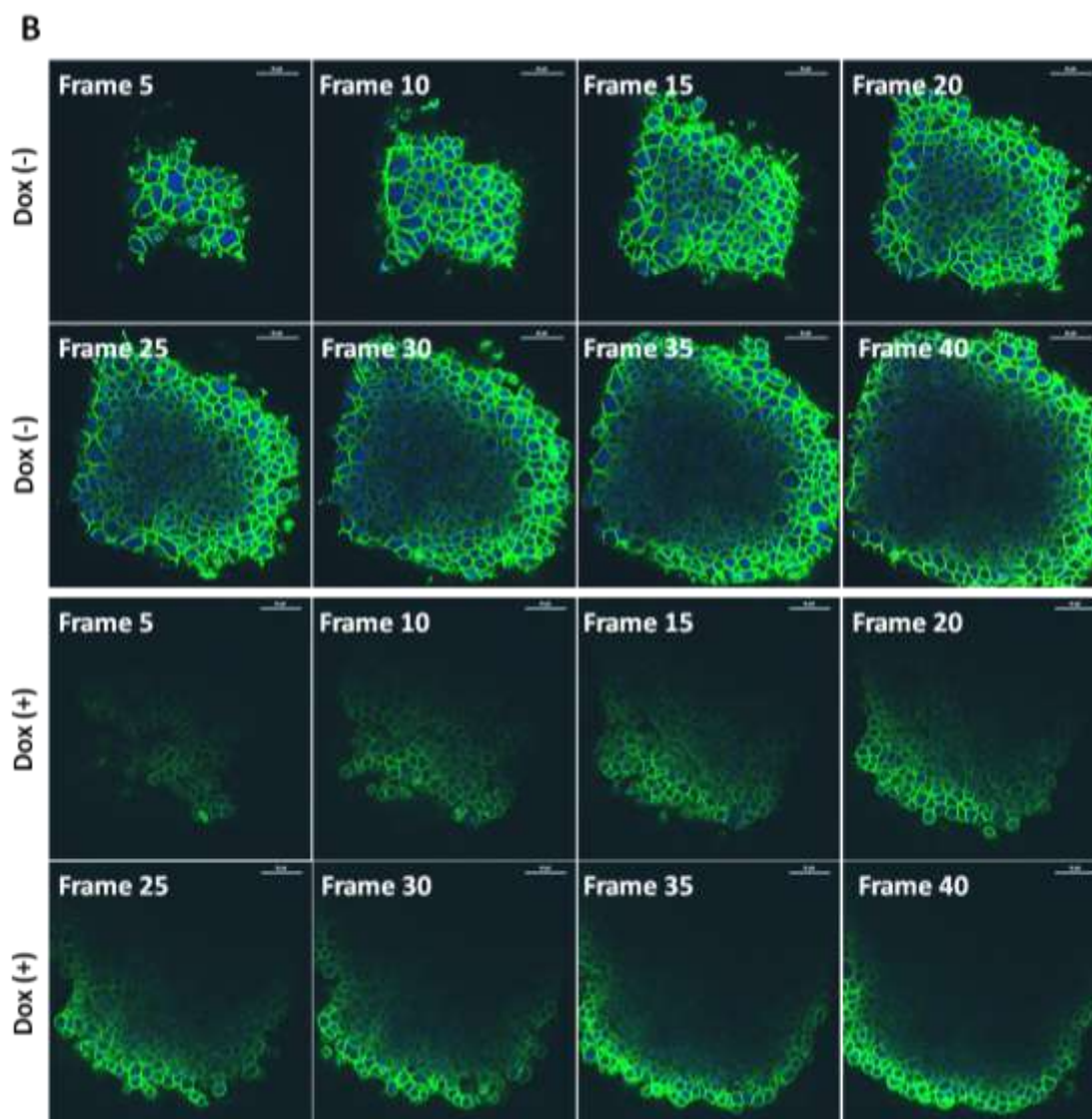


**Figure 8.** Confirmation of cell migration. (A) Boyden chamber assay of 3D structures with or without doxycyclin treatment. (B) Confocal images of 3D structures immunostained for CDH1 (green fluorescence) and nuclear (DAPI, blue color).

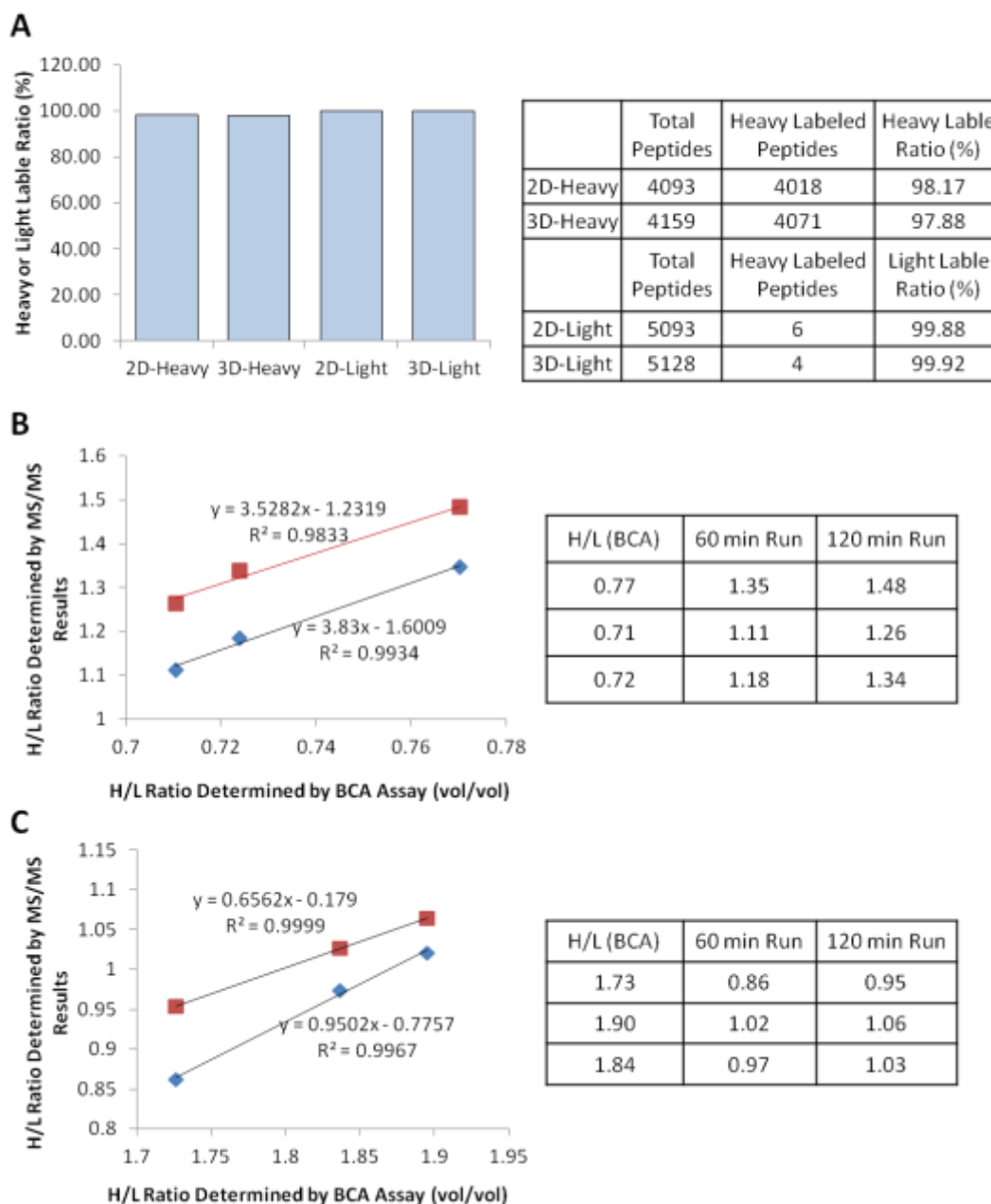
##### **5. (Task 2a) Establish the SILAC method. (7/1/2013-8/30/2013)**

During year 2, we will perform quantitative experiments to study the molecular changes of 3D structures in response to CDH1-KD induced drug resistance. We will use the SILAC label strategy to label 3D structures under different conditions, and then mix

the samples together and perform LC-MS/MS analysis. To prepare for the quantitative analysis, we first analyzed the labeling efficiency of the SILAC method. SILAC labels were checked both in 2D and 3D culturing systems. The results show that in both 2D and 3D culturing systems, for the cells cultured in media supplemented with heavy amino acids, around 98% of peptides were labeled with heavy amino acids. For the cells cultured in media supplemented with light amino acids, more than 99.8% of the peptides have light amino acids, and the presence of heavy amino acids is less than 0.2% (Figure 8A). The protein amounts in each sample were determined by BCA assay. However, because the BCA assay can sometimes generate some error, to ensure that in the real experiments the light and heavy samples can be mixed with exactly 1:1 ratio, a pre-experiment was performed to determine the actual heavy-to-light mixing ratio (vol/vol). The heavy-labeled 3D structures and light-labeled 2D layers were mixed with different volume ratios to make 1:1 total protein ratio determined by BCA assay (Figure 9B). Six samples were generated with different vol/vol ratios and tested with LC-MS/MS with 60 min run (blue line in Figure 9B) and 120 min run (red line in Figure 9B). The heavy-to-light ratio determined by LC-MS/MS showed linear correlation to the vol/vol ratios determined by BCA assay. The light-labeled 3D structures and heavy-labeled 2D labeled were tested with the same strategy and showed similar results (Figure 9C). From these linear correlations we determined the actual vol/vol ratio in order to assess the peptide heavy-to-light ratio to 1:1 for both 60 min and 120 min runs. We will use the average of these two numbers to make the heavy and light sample mixtures.

Beside this optimization, during this year, we also developed a new method for phosphoproteomic studies. Compared with the traditional and widely used methods in phosphoproteome field, our optimized method significantly decreases the required sample amount from 15mg to 3mg, without losing detection sensitivity. This approach is published in *Journal of Proteome Research*. With this approach, it will be possible to include the studies on phosphoproteomic changes caused by CDH1 knock down as well, which will further enrich our second year of research.



**Figure 9**

**Figure 9.** SILAC labeling efficiency. (A) SILAC heavy and light amino acid label efficiencies are shown in bar graph. (B, C) Validation of the ratio (vol/vol) to mix heavy and light samples to make 1:1 SILAC mixtures. (B) is for the mixture of heavy-labeled 3D structures and light-labeled 2D layers, and (C) is for the mixture of light-labeled 3D structures and heavy-labeled 2D layers.



## **6. (Task 1d) Cellular responses with/without reducing CDH1 expression. (8/1/2013-9/30/2013)**

Because of the delay of the CDH1-KD cell line establishment, we just began the experiments for this section of the project.

### **KEY RESEARCH ACCOMPLISHMENTS**

1. The colorectal cancer cell lines which can inducibly knock down CDH1 expression were successfully established.
2. Successfully established the 3D model for researching CDH1 down regulation related biological processes.
3. Successfully optimized the conditions for inducing CDH1 down regulation in 3D systems.
4. Successfully observed the morphological changes of the 3D structures when inducing CDH1 knock down.
5. Successfully optimized SILAC conditions.
6. Established a new method for phosphoproteomic studies.

### **REPORTABLE OUTCOMES**

#### **Manuscripts:**

Yue XS, Hummon AB. Combination of Multistep IMAC Enrichment with High-pH Reverse Phase Separation for In-Depth Phosphoproteomic Profiling. *J Proteome Res.* 2013 Sep 6;12(9):4176-86.

#### **Presentations:**

Yue XS, Hummon AB. Reducing Sample Size and Improving Numbers of Identified Proteins: Phosphoproteomic Studies with SCX-IMAC and IMAC-RP Methods (American Society for Mass Spectrometry conference; Minneapolis, MN; June, 2013)

Yue XS, Hummon AB. 3D Model for Studying Roles of CDH1 in EMT and Metastasis (Walther Cancer Foundation Symposium; Notre Dame IN, October 4-5, 2013)

Yue XS, Hummon AB. IMAC-RP method for Reducing Sample Size and Improving Numbers of Identified Proteins in Phosphoproteomic Studies (Midwestern Universities Analytical Chemistry Conference; Notre Dame IN, October 10-12, 2013).

Yue XS, Hummon AB. 3D Model for Studying Roles of CDH1 in EMT and Metastasis (Midwestern Universities Analytical Chemistry Conference; Notre Dame IN, October 10-12, 2013).

### **Development of cell lines:**

Developed the cell line set: HT29-Vector, HT29-Green, HT29-Blue for evaluation of CDH1 knock down effects.

## **CONCLUSION**

In the first year of research, we successfully established the inducible CDH1 knock-down cell lines with HT29 cells (HT29-Green, HT29-Blue, and HT29-Vector as negative control), and used these cell lines to establish the 3D models for investigating CDH1 knock-down induced EMT. We optimized the conditions for initiating 3D structure formation, and found the best conditions for inducing CDH1 knock-down in 3D structures. The optimal conditions are 3000 cells/well seeding density, culturing for less than 10 days, inducing with 2  $\mu\text{g/ml}$  of doxycyclin for 3 days. The CDH1 down regulation was confirmed with RT-PCR analysis, and the cell morphological changes were confirmed with SEM and confocal microscopy observation. The increase of cell migration when down regulating CDH1 was confirmed with Boyden Chamber assay. We also optimized the SILAC methods and developed a new method for phosphoproteomic studies, which was published in *Journal of Proteome Research*.

In conclusion, during the first year, we accomplished most of the work we proposed in our original proposal, and finished the first part of the second year's tasks. The first year's research provided us a good start and foundation for our later work.

## REFERENCES

- [1] Kang Y, Massagué J. Epithelial-mesenchymal transitions: twist in development and metastasis. *Cell*. 2004; 118(3):277-9.
- [2] Yilmaz M, Christofori G. EMT, the cytoskeleton, and cancer cell invasion. *Cancer Metastasis Rev*. 2009; 28(1-2):15-33.
- [3] Lu MH, Huang CC, Pan MR, Chen HH, Hung WC. Prospero homeobox 1 promotes epithelial-mesenchymal transition in colon cancer cells by inhibiting E-cadherin via miR-9. *Clin Cancer Res*. 2012; 18(23):6416-25.
- [4] McConkey DJ, Choi W, Marquis L, Martin F, Williams MB, Shah J, Svatek R, Das A, Adam L, Kamat A, Siefker-Radtke A, Dinney C. Role of epithelial-to-mesenchymal transition (EMT) in drug sensitivity and metastasis in bladder cancer. *Cancer Metastasis Rev*. 2009; 28(3-4):335-44.
- [5] Voulgari A, Pintzas A. Epithelial-mesenchymal transition in cancer metastasis: mechanisms, markers and strategies to overcome drug resistance in the clinic. *Biochim Biophys Acta*. 2009; 1796(2):75-90.
- [6] Frisch SM, Schaller M, Cieply B. Mechanisms that link the oncogenic epithelial-mesenchymal transition to suppression of anoikis. *J Cell Sci*. 2013; 126(Pt 1):21-9.
- [7] Ilya Serebriiskii, Remedios Castelló-Cros, Acacia Lamb, Erica A. Golemis, Edna Cukierman. Fibroblast-derived 3D matrix differentially regulates the growth and drug-responsiveness of human cancer cells. *Matrix Biol*. 2008; 27(6): 573–585.
- [8] Baharvand H, Hashemi SM, Kazemi Ashtiani S, Farrokhi A. Differentiation of human embryonic stem cells into hepatocytes in 2D and 3D culture systems in vitro. *Int J Dev Biol*. 2006; 50(7):645-52.
- [9] Han J. and Chang H., et al. Multiscale iterative voting for differential analysis of stress response for 2D and 3D cell culture models. *J Microsc* 2011; 241(3): 315-26.
- [10] Mishra, DK. and Sakamoto JH, et al. Human lung cancer cells grown in an ex vivo 3D lung model produce matrix metalloproteinases not produced in 2D culture. *PLoS One* 2012; 7(9): e45308.
- [11] Chitcholtan K. and Asselin E., et al. Differences in growth properties of endometrial cancer in three dimensional (3D) culture and 2D cell monolayer. *Exp Cell Res*. 2013; 319(1): 75-87.

**Table 3.** Diameters and standard deviations of HT29 3D structures after culturing for different days.

cell size	2	3	4	5	6	7	8	9	10	11	12	13	14	15	16	17	18	19	20	21	22	23	24	26	28	30	32	34	36
500	209	237	265	309	361	419	477	547	595	640	679	716	751	773	798	805	837	841	887	909	923	927	941	916	924	933	952	1018	1063
1000	250	278	313	359	421	481	529	587	627	663	704	728	760	772	782	782	819	823	823	861	854	851	863	860	844	840	843	913	956
3000	374	387	428	472	527	576	611	649	675	693	729	737	741	752	758	756	773	763	743	750	741	738	751	746	716	720	764	827	909
5000	447	466	498	535	587	635	656	687	696	720	721	735	749	758	757	750	760	746	751	747	725	733	678	734	707	642	756	761	895
7000	504	509	548	577	622	673	680	699	716	721	730	739	729	731	740	720	715	708	722	709	693	703	697	705	669	665	693	784	867
9000	563	562	591	627	673	708	727	726	753	749	760	753	763	743	751	730	744	729	733	734	723	720	712	711	695	680	724	810	873
11000	581	591	619	658	712	739	753	760	753	758	773	768	780	761	752	742	728	735	722	730	717	715	715	710	701	681	723	813	886
13000	605	613	641	679	723	744	755	753	748	744	747	740	751	727	727	706	711	708	713	703	686	696	698	686	680	662	721	778	848
15000	644	641	666	706	754	774	766	774	766	760	747	747	739	743	721	712	719	708	702	698	689	693	703	692	672	655	680	822	835
30000	769	745	754	771	798	818	820	801	773	757	735	734	710	707	704	692	679	672	687	661	654	646	656	647	622	612	616	723	794
60000	958	920	916	922	947	946	917	892	862	849	819	804	795	782	778	761	752	753	745	729	714	708	722	723	698	679	739	822	900
100000	1189	1121	1088	1125	1136	1123	1055	1015	932	911	886	866	837	829	805	778	763	763	741	730	714	709	708	705	666	655	721	803	874
std	2	3	4	5	6	7	8	9	10	11	12	13	14	15	16	17	18	119	20	21	22	23	24	26	28	30	32	34	36
500	9.7	11.1	9.3	7.4	11.1	13.4	15.8	10.8	15.1	21.0	20.3	24.0	40.1	38.7	37.0	32.5	38.6	43.3	39.3	48.7	62.5	44.0	62.2	49.9	65.3	62.5	52.6	38.8	53.9
1000	7.1	16.3	12.2	10.6	12.1	12.7	17.2	13.6	14.3	18.7	23.5	22.9	25.9	32.6	24.4	26.0	32.5	32.8	37.6	58.0	64.0	61.7	69.9	61.4	69.0	71.6	59.0	55.5	48.8
3000	11.2	11.8	11.0	11.2	15.6	16.1	13.4	14.3	24.2	21.0	22.7	24.8	34.1	29.4	27.4	26.2	20.2	26.3	15.4	20.0	17.2	13.8	22.8	27.1	25.3	29.3	77.8	42.2	55.2
5000	9.1	11.0	8.5	12.7	9.0	15.0	9.6	13.0	13.7	12.8	16.8	16.7	28.3	32.7	19.6	21.4	36.7	21.8	25.5	23.8	24.8	23.0	29.8	17.7	16.7	28.9	25.0	45.8	42.2
7000	21.0	18.7	12.4	12.0	16.6	12.5	11.2	15.5	20.0	23.2	20.0	31.7	36.9	30.3	36.8	29.0	30.6	27.5	36.0	35.8	34.1	35.9	23.4	28.7	29.4	40.2	35.9	36.5	37.5
9000	17.5	14.9	9.4	11.6	17.1	14.7	20.8	20.0	27.9	29.8	21.1	31.9	27.9	24.1	27.6	29.0	37.7	30.9	34.6	25.7	24.9	31.5	27.3	25.1	32.0	34.1	50.4	36.3	53.2
11000	12.0	12.1	14.2	15.0	14.9	16.2	15.1	14.8	20.8	20.4	21.1	14.2	18.6	14.7	21.5	19.6	21.6	19.7	18.1	32.0	26.2	27.9	24.8	20.7	28.1	24.0	30.4	30.0	34.4
13000	11.6	13.3	8.8	11.1	13.0	13.9	15.2	20.3	9.9	21.5	15.0	9.6	19.9	19.9	25.1	21.6	23.4	22.5	22.2	28.6	25.0	27.5	29.8	27.3	27.9	39.2	58.6	35.5	52.5
15000	15.6	7.3	12.4	9.4	15.8	14.6	25.6	23.7	23.9	22.7	29.0	23.7	25.0	27.7	26.9	29.3	29.4	21.3	25.3	17.9	18.3	15.2	15.4	27.7	21.0	18.9	38.7	78.1	59.9
30000	20.8	15.4	14.0	19.4	32.5	20.3	34.0	38.3	56.3	51.2	56.4	48.3	51.7	57.8	53.9	57.0	62.5	61.9	79.9	75.2	89.5	84.4	89.1	75.9	85.5	86.9	65.9	59.7	68.3
60000	32.1	27.3	36.6	30.6	56.1	70.4	34.7	36.0	62.4	67.4	59.3	60.0	52.2	41.8	44.5	39.1	45.4	50.0	36.2	52.0	41.3	44.1	47.3	39.3	56.4	42.8	35.1	41.1	62.9
100000	38.8	27.6	37.3	26.0	55.7	61.9	44.1	36.8	20.2	41.6	47.2	50.0	52.2	41.7	55.7	52.5	66.4	44.0	85.3	83.0	96.0	73.8	55.7	54.6	73.4	69.0	67.9	99.8	69.7

**Table 4.** Diameters and standard deviations of HCT116 3D structures after culturing for different days.

CellSize	2	3	4	5	6	7	8	9	10	11	12	13	14	15	16	17	18	19	20	21	22	23	24	26	28	30	32	34
500	234	274	332	386	475	522	585	665	692	753	796	821	867	895	879	880	881	884	874	881	890	888	873	843	771	726	694	718
1000	305	340	396	440	505	570	627	695	726	749	765	776	784	806	792	799	795	796	773	754	758	761	735	667	597	565	564	528
3000	470	508	555	575	664	695	714	742	741	763	767	772	745	747	742	742	725	728	694	684	685	658	640	604	530	495	485	523
5000	569	609	638	649	735	766	776	797	779	797	781	788	752	751	729	730	708	698	662	597	587	579	524	493	444	435	435	475
7000	636	674	694	717	762	793	779	823	779	765	748	754	733	731	700	695	677	655	612	583	572	561	547	466	434	429	410	443
9000	702	737	754	773	850	855	828	848	812	826	782	777	738	732	722	712	698	676	664	613	574	563	561	489	429	399	413	462
11000	761	795	802	804	851	864	834	849	847	847	819	807	782	769	754	748	727	709	680	607	592	574	559	516	490	513	492	439
13000	772	811	826	835	864	871	833	861	829	831	812	806	773	771	733	733	694	682	639	595	578	563	547	494	459	438	440	448
15000	832	841	844	856	892	884	837	849	822	813	779	785	756	737	713	711	686	675	630	564	550	551	535	507	476	469	483	477
30000	1053	1031	1018	1006	1026	1019	928	941	868	860	833	817	781	772	743	729	697	666	624	575	570	544	524	482	438	424	423	478
60000	1309	1230	1190	1173	1184	1196	1051	1037	938	928	874	858	805	763	731	705	679	663	619	549	544	524	510	479	441	446	440	446
100000	1504	1393	1335	1297	1290	1304	1203	1170	1044	995	861	831	766	738	677	653	601	591	538	508	495	485	467	444	399	456	511	547
Std	2	3	4	5	6	7	8	9	10	11	12	13	14	15	16	17	18	19	20	21	22	23	24	26	28	30	32	34
500	13.2	13.3	9.8	7.6	15.8	34.6	34.2	21.9	30.1	32.7	58.6	36.1	55.6	81.3	71.2	69.7	36.1	52.4	74.4	74.7	66.9	71.8	68.4	71.9	84.1	102.3	101.7	156.9
1000	15.7	16.2	15.2	17.3	14.7	27.8	26.7	39.3	30.6	40.9	41.7	42.1	40.9	39.9	44.6	44.1	45.0	50.5	48.9	60.9	77.0	74.9	85.4	77.9	89.3	88.4	88.6	67.7
3000	32.0	14.0	19.3	20.4	24.2	19.6	23.9	23.7	28.5	24.4	30.7	27.9	38.4	34.8	36.7	34.2	33.9	35.5	29.5	34.8	35.8	55.8	56.3	81.7	79.5	83.5	85.1	103.8
5000	17.2	13.7	6.6	15.5	18.2	30.9	28.4	32.4	24.5	35.0	36.5	37.6	30.2	15.8	21.6	26.1	34.9	43.9	44.3	55.6	61.4	68.9	142.9	65.1	58.1	56.1	56.9	60.5
7000	31.9	21.8	16.3	22.2	31.6	30.0	47.9	30.0	29.4	22.5	27.2	30.1	21.2	27.7	28.3	41.8	47.3	46.7	59.2	76.8	78.2	74.8	77.7	44.1	23.7	32.5	29.5	48.7
9000	25.4	21.2	19.9	28.4	32.7	58.6	54.4	58.7	61.2	47.5	42.6	51.8	28.3	36.1	42.8	37.3	38.2	36.3	22.0	61.8	60.5	57.8	54.7	41.9	103.0	93.0	110.4	133.9
11000	32.2	21.0	24.2	17.2	28.1	41.2	40.0	34.5	31.7	25.8	35.3	26.8	29.9	27.5	22.0	32.7	42.7	44.5	45.6	66.8	54.9	53.8	56.1	81.9	55.7	143.4	132.6	40.4
13000	26.7	25.5	23.4	15.6	39.2	47.2	41.9	30.5	32.3	26.4	24.5	19.5	31.0	25.7	27.9	24.1	61.9	68.3	80.3	89.5	85.9	67.6	64.1	57.4	65.4	45.4	39.1	70.3
15000	19.6	25.0	24.9	18.2	30.5	37.6	41.6	36.9	43.6	36.7	22.0	32.7	50.8	50.3	42.8	37.1	44.5	53.0	53.0	72.7	75.8	71.9	84.5	73.0	85.1	104.6	98.8	81.5
30000	28.6	20.0	14.1	25.1	41.2	38.2	31.6	16.4	35.8	32.6	24.0	20.3	31.7	36.3	38.8	40.6	54.7	56.1	69.6	81.0	72.1	64.6	67.8	65.6	74.5	72.3	57.0	51.8
60000	36.9	37.8	41.3	45.3	41.5	53.5	50.8	45.7	39.9	38.1	56.7	52.9	63.7	89.3	81.8	91.5	94.5	77.4	83.8	67.5	59.5	54.1	48.0	43.9	50.3	47.7	50.7	126.2
100000	23.1	17.2	31.3	27.7	30.3	37.0	47.2	34.1	46.3	49.5	61.2	45.9	55.5	41.5	49.2	39.3	40.7	59.1	46.5	46.5	33.0	22.2	32.1	25.3	39.3	60.7	66.3	87.4

# Combination of Multistep IMAC Enrichment with High-pH Reverse Phase Separation for In-Depth Phosphoproteomic Profiling

Xiao-Shan Yue and Amanda B. Hummon\*

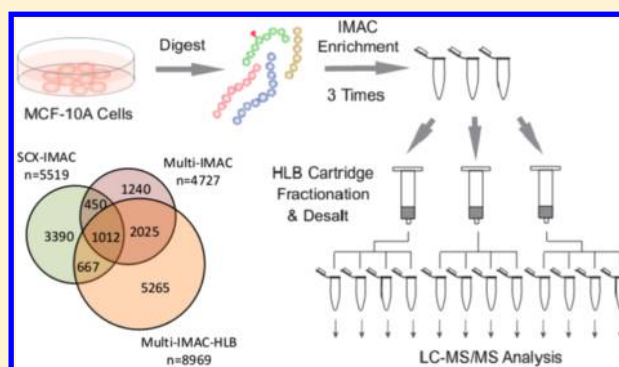
Department of Chemistry and Biochemistry, University of Notre Dame, 251 Nieuwland Science Hall, Notre Dame, Indiana 46556, United States

**S** Supporting Information

**ABSTRACT:** Typical mass spectrometric phosphoproteome studies are complicated by the need for large amounts of starting material and extensive sample preparation to ensure sufficient phosphopeptide identifications. In this paper, we present a novel strategy to perform optimized multistep IMAC enrichment from whole cell lysates followed by high-pH reverse phase fractionation (multi-IMAC-HLB; HLB means hydrophilic–lipophilic-balanced reversed-phase cartridge). The peptide-to-IMAC ratio was optimized to maximize IMAC performance, while multistep IMAC enrichment enabled improved phosphopeptide acquisition. The addition of the HLB step further fractionates the IMAC enriched phosphopeptides while desalting the samples, which dramatically reduces the sample manipulation time and sample loss compared to other popular strategies. We compared the phosphopeptide identification results of the multi-IMAC-HLB method with 3 mg of starting material to the well-established SCX-IMAC method with 15 mg of starting material. We identified 8969 unique phosphopeptides with the multi-IMAC-HLB method, compared to 5519 unique phosphopeptides identified with the SCX-IMAC method, an increase of 62.5%. The increase in the numbers of identified phosphopeptides is due to the increase in the ratio of identified phosphopeptides out of all detected peptides, 70.5% with multi-IMAC-HLB method compared to 32.3% with the SCX-IMAC method. Multi-IMAC-HLB is a robust and efficient method for in-depth phosphoproteomic research.

We compared the phosphopeptide identification results of the multi-IMAC-HLB method with 3 mg of starting material to the well-established SCX-IMAC method with 15 mg of starting material. We identified 8969 unique phosphopeptides with the multi-IMAC-HLB method, compared to 5519 unique phosphopeptides identified with the SCX-IMAC method, an increase of 62.5%. The increase in the numbers of identified phosphopeptides is due to the increase in the ratio of identified phosphopeptides out of all detected peptides, 70.5% with multi-IMAC-HLB method compared to 32.3% with the SCX-IMAC method. Multi-IMAC-HLB is a robust and efficient method for in-depth phosphoproteomic research.

**KEYWORDS:** phosphoproteomics, multistep IMAC enrichment, high-pH reverse phase fractionation, SCX fractionation, high pI phosphopeptides



## INTRODUCTION

Proteins are widely modified with posttranslational modifications (PTMs) such as phosphorylation, methylation, glycosylation, and ubiquitination. Phosphorylation is a reversible modification and is commonly involved in regulating cellular processes such as proliferation, apoptosis, differentiation, migration, and tumor metastasis.<sup>1,2</sup> Phosphorylation and dephosphorylation can activate or deactivate signaling molecules, thus controlling many signaling pathways. Global phosphoproteomic studies can provide an overall image of cellular phosphorylation status at certain time points and have a high potential for screening biological markers and targets for disease diagnosis and treatment.<sup>3,4</sup> However, because of the low abundance of phosphoproteins and high variability of phosphorylation sites, in-depth phosphoproteomic studies commonly suffer from two major problems: (1) the need to enrich for phosphoproteins/phosphopeptides from protein/peptide mixtures; and (2) the careful fractionation of the protein/peptide mixtures to reduce the sample complexity prior to LC–MS analysis. Many methods for phosphopeptide enrichment and fractionation have been reported including enrichment with immobilized metal affinity chromatography (IMAC),<sup>5</sup> polymer-based metal ion affinity capture (Poly-

MAC),<sup>6</sup> titanium dioxide (TiO<sub>2</sub>),<sup>7</sup> polymer-oxotitanium-modified gold wafer (Au–P–oxoTi),<sup>8</sup> and fractionation with strong cation exchange (SCX),<sup>9</sup> strong anion exchange (SAX),<sup>10</sup> electrostatic repulsion-hydrophilic interaction chromatography (ERLIC),<sup>11</sup> and hydrophilic interaction chromatography (HILIC).<sup>12</sup> The combination of different fractionation methods with diverse enrichment approaches have been utilized in many phosphoproteomic studies.<sup>13–16</sup> In most of these studies, the phosphopeptides were enriched after the fractionation steps, though some reports suggest that the order of operations does not affect the number of phosphopeptides identified.<sup>17</sup>

The combination of SCX separation followed by IMAC enrichment is a widely used two-dimensional approach in phosphoproteomic studies.<sup>18–21</sup> This method typically includes many steps including tryptic digestion, an initial desalting step, a first lyophilization, SCX, a second lyophilization, a second desalting step, a third lyophilization, IMAC, a third desalting step, and then the samples are analyzed by LC–MS (Figure 1).<sup>18</sup> Many studies using this method report good identification

Received: June 4, 2013

Published: July 23, 2013

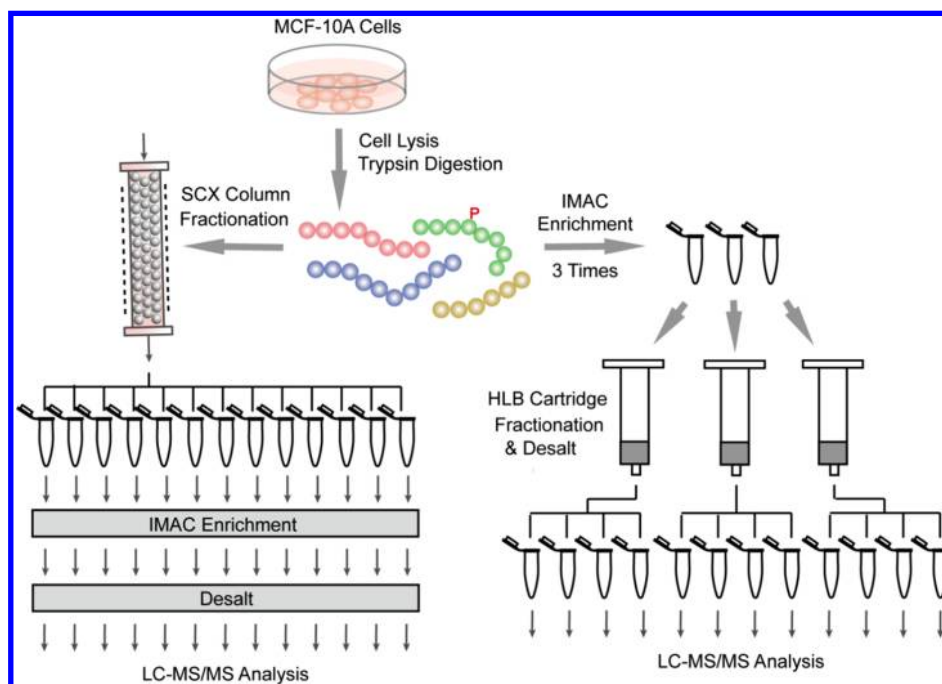


**Figure 1.** Workflow of SCX-IMAC and multi-IMAC-HLB methods.

of large numbers of phosphopeptides.<sup>19–21</sup> However, because there are so many steps in the SCX-IMAC method and each step can result in material loss, a large amount of starting material is required. The typical starting material for an SCX-IMAC procedure is 15–20 mg of cell/tissue digest,<sup>18</sup> which is difficult to achieve if working with precious tissue samples and is expensive even when working with established cell lines. The approach is even more expensive when combined with SILAC or iTRAQ labeling quantification strategies. Also, it is hard to control the amount of peptides in each fraction, which results in a different peptide-to-IMAC ratio in each fraction, leading to relatively low phosphopeptide enrichment efficiencies in some fractions.

Online high-pH reverse phase (RP) separation is another fractionation method used prior to LC–MS analysis in proteomic research.<sup>22–24</sup> The benefit of this method is that samples are desalted while performing the fractionation, which reduces the sample manipulation steps and decreases the experimental time and effort. Currently, to the best of our knowledge, only a handful of researchers have reported using the high-pH RP separation for phosphoproteomic research,<sup>25</sup> and no research has been published comparing the high-pH RP separation method with the popular low-pH separation methods such as SCX for phosphoproteomic research.

In this paper, we optimize the IMAC enrichment conditions and evaluate the phosphoproteome of the human mammary cell line, MCF-10A, using both SCX-IMAC and our optimized multistep IMAC enrichment followed by the high-pH RP fractionation method (multi-IMAC-HLB). We identified 5519 unique phosphopeptides in 13 fractions using the SCX-IMAC method from 15 mg of starting material. As a comparison, using only 3 mg of starting material, 8969 unique phosphopeptides were identified in 12 multi-IMAC-HLB fractions. We evaluate the efficiency of the SCX-IMAC method, the multistep IMAC enrichment method, and the multi-IMAC-HLB method by comparing the number of identified unique phosphopeptides, the phosphopeptide ratios, the numbers of singly and multiply

phosphorylated peptides, the numbers of phosphosites identified, the distribution of phospho-Serine (p-Ser), phospho-Threonine (p-Thr), and phospho-Tyrosine (p-Tyr) sites, and the detected charge states for each method. We also compare the pI values and grand average of hydropathy (GRAVY) values of the identified phosphopeptides with the SCX-IMAC or the multi-IMAC-HLB method.

## ■ MATERIALS AND METHODS

### Chemicals and Materials

A list of reagents is provided in the Supporting Information.

### Cell Culture and Trypsin Digestion

MCF-10A cells were cultured in DMEM/F12 (with 15 mM HEPES buffer) media supplemented with 5% horse serum, 0.01 mg/mL pf insulin, 20 ng/mL of EGF, 100 ng/mL of cholera toxin, and 500 ng/mL of hydrocortisone. After growing to 80% confluence, cells were rinsed twice with ice-cold PBS and lysed with 8 M urea lysis buffer, which contained the final concentration of 8 M urea, 75 mM NaCl, 50 mM Tris-HCl (pH8.2), 1 mM NaF, 1 mM  $\beta$ -glycerophosphate, 1 mM sodium orthovanadate, 10 mM sodium pyrophosphate, 1 mM PMSF, and 1 tablet of EDTA-free protease inhibitors cocktail for every 10 mL of lysis buffer. Cell lysates were sonicated for 1 min followed by a 2 min rest interval, and this operation was repeated for 3 times. The mixture was centrifuged at 2500g for 10 min to remove cell debris. Protein concentrations were confirmed with bicinchoninic acid (BCA) protein assay kit (Thermo Scientific Pierce, Rockford, IL), and 15 mg of protein was used in the SCX-IMAC experiment, while 3 mg of protein was used in multistep IMAC enrichment and multi-IMAC-HLB experiments. Proteins were treated with 5 mM DTT for 25 min at 56 °C to reduce their disulfide bonds. Then IAA was added to the protein mixtures to make a final concentration of 14 mM and reacted in the dark for 30 min at room temperature to allow alkylation of the cysteines. Another 5 mM DTT was added and allowed to react in the dark for 15 min to stop the



IAA reaction. The protein mixture was then diluted with 25 mM Tris-HCl (pH 8.2) to achieve a final urea concentration of 1.8 M. Proteins were digested overnight with trypsin from bovine pancreas (Sigma-Aldrich, St Louis, MO) at 37 °C at a 50:1 protein to trypsin ratio (m/m) in the presence of 1 mM  $\text{CaCl}_2$ . The digestion reaction was stopped by adding TFA to a final concentration of 0.4% (v/v). Samples were centrifuged at 2500g for 10 min to remove any precipitates. The peptides were then desalted by 500 mg reverse-phase tC18 Sep-Pak solid-phase extraction cartridges (Waters Corporation, Milford, MA) as reported previously.<sup>18</sup>

### Strong Cation Exchange (SCX)

The SCX steps were performed as described previously.<sup>18</sup> Briefly, 15 mg of desalted peptides were resuspended in 500  $\mu\text{L}$  of SCX Buffer A (30% ACN, 7 mM  $\text{KH}_2\text{PO}_4$ , pH 2.65) and loaded onto PolySULFOETHYL A column (9.4  $\times$  200 mm, 5  $\mu\text{m}$  particle size, 200 Å pore size) (PolyLC, Columbia, MD) with 5 injections. The separations were performed on a Waters Alliance e2695 System (Waters Corporation, Milford, MA) at a flow rate of 1 mL/min. Liquid chromatography runs (120 min total time) included 2 min at 100% Buffer A, 33 min of a gradient from 0 to 25% Buffer B (30% ACN, 7 mM  $\text{KH}_2\text{PO}_4$ , 350 mM KCl, pH 2.65), 1 min of a jump from 35 to 100% Buffer B, 5 min of running at 100% Buffer B, 6 min of washing with 100% water, 11 min of washing with 100% Buffer C (50 mM  $\text{K}_2\text{HPO}_4$ , 500 mM NaCl, pH 7.5), 6 min of washing with 100% water, and 52 min of equilibration with 100% Buffer A. The chromatogram was recorded at 220 and 280 nm. The eluates from the first 52 min were collected at 4 min intervals to generate 13 fractions. The SCX fractions were then lyophilized to reduce the volume by 30% and desalted with 100 mg reverse-phase tC18 Sep-Pak solid-phase extraction cartridges (Waters Corporation, Milford, MA).

### IMAC Enrichment

For the SCX-IMAC work flow, the IMAC enrichment was performed as previously reported.<sup>18</sup> The required amounts of Phos-Select iron affinity gel (IMAC beads) (Sigma-Aldrich, St Louis, MO) were washed 3 times with a 10 $\times$  volume of IMAC binding buffer (40% ACN, 25 mM FA in  $\text{H}_2\text{O}$ ) and resuspended in IMAC binding buffer to make a 50% gel slurry. The lyophilized and desalted SCX fractions were resuspended in 120  $\mu\text{L}$  of IMAC binding buffer and incubated with 10  $\mu\text{L}$  of IMAC slurry at room temperature for 60 min with vigorous shaking. Incubated IMAC beads were then washed with 120  $\mu\text{L}$  of IMAC binding buffer 3 times to remove any nonspecific binding. Phosphopeptides were then eluted with 40  $\mu\text{L}$  elution buffer (50 mM  $\text{K}_2\text{HPO}_4/\text{NH}_4\text{OH}$ , pH10) 3 times by incubating at room temperature for 5 min while shaking. Formic acid, 40  $\mu\text{L}$  of a 10% solution, was added immediately after elution to acidify the solution. The eluates were then lyophilized and desalted with C18 ZipTips (Millipore, Billerica, MA) according to the manufacturer's instructions. For optimizing IMAC conditions, different amounts of IMAC slurries were added to 3 mg of peptides according to the indicated peptide-to-IMAC ratio ( $\mu\text{g}/\mu\text{L}$ ). The enrichment was carried out in the same way as described above. For the multistep IMAC enrichment, phosphopeptides were enriched from 3 mg of peptides with the optimized 100:1 peptide-to-IMAC ratio. The second cycle of IMAC enrichment was performed with IMAC flow-through of the first cycle of IMAC enrichment, while the third cycle of IMAC enrichment was performed with the IMAC flow-through from the second cycle

of IMAC enrichment. The eluates from the multistep IMAC enrichment were either desalted with C18 ZipTips for LC-MS/MS analysis, or used with high-pH reverse phase HLB desalting/fractionation.

### High-pH Reverse Phase HLB Separation

The high pH reverse phase separation was carried out with OASIS HLB 1 cc Vac Cartridge with 30 mg sorbent per cartridge and 30  $\mu\text{m}$  of particle size (Waters Corporation, Milford, MA). All buffers used in HLB separation contained 10 mM  $\text{NH}_4\text{HCO}_3$  and were adjusted to pH 10 with  $\text{NH}_4\text{OH}$ . After washing with 3 mL of 80% ACN/ $\text{NH}_4\text{HCO}_3$  and equilibrating with 3 mL of 1% ACN/ $\text{NH}_4\text{HCO}_3$ , IMAC enriched samples were conditioned with 0.5 mL of 1% ACN/ $\text{NH}_4\text{HCO}_3$  and loaded onto the equilibrated HLB columns. The samples were then washed with 3 mL of 1% ACN/ $\text{NH}_4\text{HCO}_3$  to remove the salts introduced during the IMAC enrichment. Serial elution was carried out stepwise with 0.5 mL of each elution buffer in the order of 5, 10, 15, 20, 25, 30, 35, and 80% ACN/ $\text{NH}_4\text{HCO}_3$ . Eluates were passed into an Eppendorf tube containing 25  $\mu\text{L}$  of 100% FA to acidify and stabilize the phosphopeptides. Forced air was used to accelerate the buffers passing through the cartridges. To reduce the LC-MS/MS analysis time, fraction numbers were reduced by combining the 5 and the 25% ACN/ $\text{NH}_4\text{HCO}_3$  fractions. The 10 and the 30% fractions, the 15 and the 35% fractions, and the 20 and 80% fractions were also combined. The resulting HLB fractions were lyophilized and desalted with ZipTips before LC-MS/MS analysis. ZipTips were not used if working with trap column.

### Mass Spectrometric Analysis

Before liquid chromatography electrospray ionization tandem mass spectrometry (LC-ESI-MS/MS) analysis, all samples were lyophilized and resuspended in MS loading buffer (1% HPLC grade ACN, 0.1% FA in HPLC grade water). The mass spectrometric analysis was performed on a Q-Exactive mass spectrometer (Thermo Fisher Scientific, Bremen, Germany) coupled with a nanoACQUITY Ultra Performance LC (UPLC) system (Waters Corporation, Milford, MA). Peptides were loaded onto a C18 reverse phase column (100  $\mu\text{m}$   $\times$  100 mm, 1.7  $\mu\text{m}$  particle size, BEH130) (Waters Corporation, Milford, MA) with 97% buffer A (0.1% FA in water) and 3% buffer B (0.1% FA in ACN). Peptide separation was carried out with a 73-min linear gradient from 3 to 30% buffer B, then maintained at 85% buffer B for 5 min and re-equilibrated with 3% buffer B for 10 min before the next run. The flow rate was 1200 nL/min. The Q-Exactive was equipped with a nanoelectrospray ion source operating at a source voltage of 1.8 kV and the ion transfer tube temperature of 280 °C. The full MS scans were acquired in the Orbitrap mass analyzer with an  $m/z$  range of 350–1800, at the mass resolution of 70000 at  $m/z$  = 200. Automatic gain control (AGC) target value was set to  $1 \times 10^6$ , with a maximum fill time of 250 ms. For the MS/MS method, the top 12 most intense parent ions were selected with an isolation window of 2.0  $m/z$  and fragmented under a normalized collision energy (NCE) of 30%, with the AGC target value of  $1 \times 10^6$  and the maximum fill time of 120 ms. The parent ions with unassigned charges or a charge state of  $z = 1$  were excluded from fragmentation. The intensity threshold for selection was set to  $8.3 \times 10^4$ . The fragmentation was performed in an HCD collision cell with a mass resolution of 35000 at  $m/z$  = 200 and a dynamic exclusion period of 20 s after 1 repeat count. All samples were run in technical duplicate.



## Data Analysis

All .raw files acquired with the Q-Exactive were searched with Proteome Discoverer 1.3 software (Thermo Fisher Scientific, Bremen, Germany) using MASCOT 2.2.4 as a search algorithm and against the SwissProt human database modified by adding common contamination sequences (updated on 05/2012, 86 758 sequences). The peptide false discovery rate (FDR) was determined by searching against the corresponding reverse database. The searches were carried out with precursor peptide mass tolerance of 10 ppm and fragment ion mass tolerance of 0.02 Da, and allow up to two missed cleavages with trypsin digestion. Carbamidomethylation of cysteine was set as a fixed modification, while oxidation of methionine and phosphorylation of serine, threonine and tyrosine were set as variable modifications. Search results were screened with an FDR value of 0.01, and phosphopeptides with PhosphoRS score higher than 0.99 were considered to have confident phosphosite localization. Peptides with the same sequence but different oxidation states were treated as the same peptide considering that the oxidation could have been introduced during sample manipulation. The peptide lists were exported to Microsoft Excel and processed with Excel or in-house scripts. The 4-circle Venn diagrams were generated by the online tool Venny (Oliveros, J.C. 2007, <http://bioinfo.gp.cnb.csic.es/tools/venny/index.html>). The 3-circle proportional Venn diagrams were generated by CircleApplet, which can be down loaded from <https://www.cs.kent.ac.uk/people/staff/pjr/EulerVennCircles/EulerVennApplet.html>. The GRAVY values were calculated by the GRAVY calculator (<http://www.gravy-calculator.de/>). The pI values of phosphopeptides were calculated using pI Calculator (<https://trac.nbic.nl/picalculator/>).<sup>26</sup> ExPASy pK<sub>a</sub> values of amino acids were used for the calculation, and pK<sub>a</sub> values for the phospho- groups were set as pK<sub>a</sub>1 = 2.12 and pK<sub>a</sub>2 = 7.21.

## RESULTS AND DISCUSSION

### Phosphopeptide Ratio Is Dependent on Peptide-to-IMAC Ratio

As a pre-experiment and a comparison standard, we used the well-established method that combines SCX and IMAC enrichment to detect phosphopeptides in the MCF-10A cell line. Thirteen SCX fractions were collected and further enriched with IMAC beads as previously reported.<sup>18</sup> (Supporting Information Figure S1) With this method, we successfully detected 5519 unique phosphopeptides and 4989 unique phosphosites with confident localization (with phosphoRS score  $\geq 0.99$ ) (Supporting Information Figure S2 and Table S1). However, the main drawback of the SCX-IMAC method is the need for a large amount of starting material to ensure sufficient numbers of identified phosphopeptides; typically more than 15 mg of starting materials is required. Possible reasons for the large amount of starting material include the following: (1) phosphopeptides are a relatively small percentage of the total number of peptides and therefore require large amounts of material to ensure the detection of phosphopeptides with low abundance, and (2) there are numerous steps in the SCX-IMAC enrichment method, with each step resulting in sample loss. Another problem we observed in our data sets is the uneven distribution of phosphopeptide ratios in each SCX fraction (Supporting Information Figure S1B and Table S1). The extremely low phosphopeptide ratio in some SCX fractions reduced the overall phosphopeptide ratio to 32.4% with SCX-IMAC

method (see Figure 5B and Supporting Information Table S5). We considered a possible reason for this low ratio might be that the peptide-to-IMAC ratio in each SCX fraction is not optimized. It was reported previously that with the TiO<sub>2</sub> enrichment, the peptide-to-TiO<sub>2</sub> ratio is crucial for the phosphopeptide enrichment efficiency.<sup>27</sup> We surmised that peptide-to-IMAC ratio might also play an important role for IMAC performance. We tested 10 different peptide-to-IMAC ratios as shown in Figure 2. The results show that with the

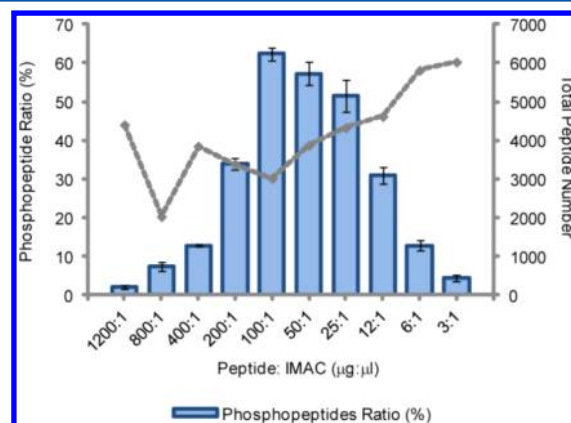


**Figure 2.** Optimization of peptide-to-IMAC ratio for IMAC enrichment. Percentage of identified phosphopeptides under different peptide-to-IMAC ratios (μg:μL) are shown in the bar graph. Identified total peptide numbers under each condition are shown with the dashed line.

100:1 (μg:μL) peptide-to-IMAC ratio, 62.3% of the total peptides retained were phosphopeptides (Figure 2, Supporting Information Table S2). At higher peptide-to-IMAC ratios, there might not be sufficient IMAC beads for enrichment, while at lower peptide-to-IMAC ratios, the nonspecific attachment of nonphosphopeptides to IMAC beads might occur. As an example, with a 3:1 peptide-to-IMAC ratio, 6025 total peptides were identified compared with 3023 peptides with a 100:1 peptide-to-IMAC ratio. However, only 244 phosphopeptides (4.6% of total) were identified with a 3:1 peptide-to-IMAC ratio, showing a dramatic decrease compared with 1827 phosphopeptides (62.3% of total) identified with a 100:1 ratio (Figure 2, Supporting Information Table S2).

Considering the large amount of required starting materials, complicated manipulation steps, and difficulties defining the total amount of peptides existing in each SCX fraction, we decided to perform enrichment directly from the whole cell lysate. An advantage of this strategy is that we knew the starting peptide amount and thus could optimize the IMAC enrichment. In addition, we anticipated that skipping the SCX fractionation steps and working with the optimized multistep IMAC enrichment would simplify the overall sample preparation process and reduce sample loss. As a result, fewer starting materials were required, and experimental time was reduced.

### Multistep IMAC Enrichment Directly from Whole Cell Lysates

To decrease the amount of starting materials needed for phosphopeptide identification and to increase the phosphopeptide enrichment efficiency, we performed direct enrichment with IMAC beads from whole cell lysate. As starting material, 3 mg of MCF-10A cell lysate were used for the IMAC

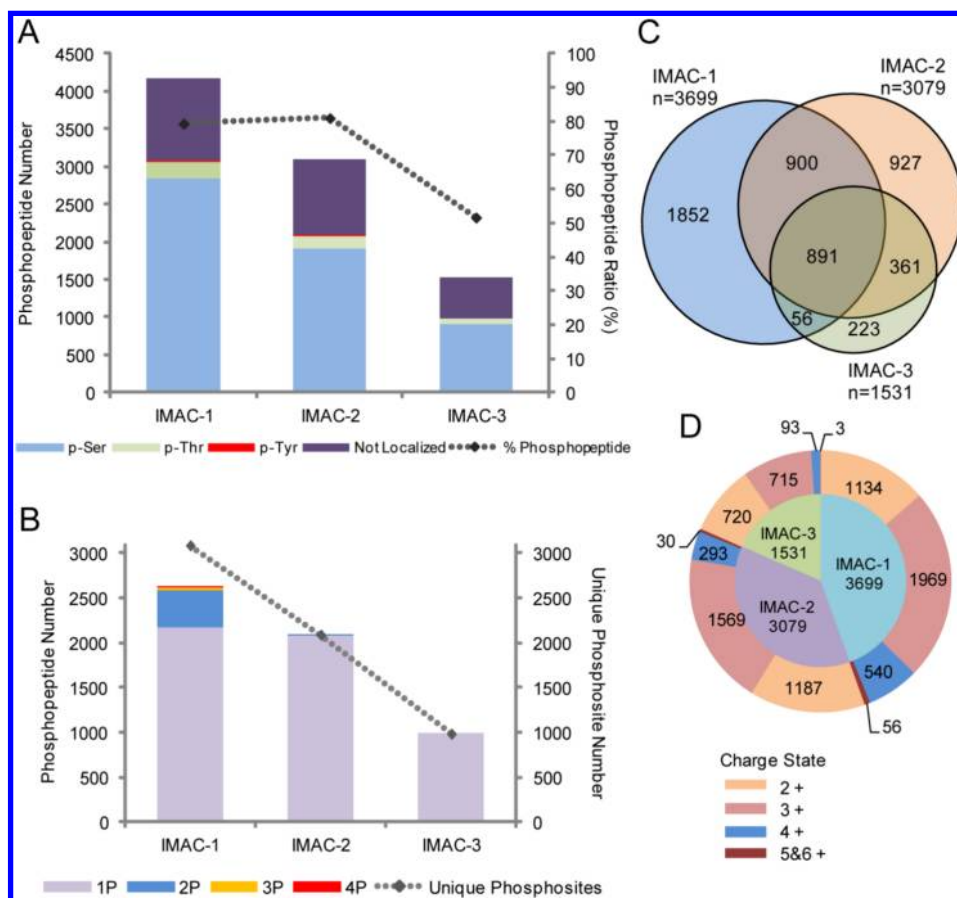


**Figure 3.** Distribution of phosphopeptides identified by multistep IMAC enrichment. (A) Numbers of identified phosphopeptides in the first, second, and third round of IMAC enrichment with phospho-serine (blue), phospho-threonine (green), or phospho-tyrosine (red) sites, and those without confident localization (phosphoRS score <99%, dark purple) are shown in the bar graph. The percentage of identified phosphopeptides from the total identified peptides in each round of IMAC enrichment are shown with the dashed line. (B) Numbers of identified phosphopeptides (phosphoRS score  $\geq 99\%$ ) with 1, 2, 3, or 4 phosphate groups are shown in the bar graph with purple, blue, yellow and red colors. Unique phosphosite numbers are calculated from phosphopeptides with phosphoRS score  $\geq 99\%$  and are shown with the dashed line. (C) Overlap of the nonredundant phosphopeptides identified in each round of IMAC enrichment are shown in the Venn diagram. (D) Charge states of phosphopeptides identified in each round of IMAC enrichment are shown in the pie chart.

enrichment. According to the optimized peptide-to-IMAC ratio, we added 30  $\mu$ L of the IMAC bead slurry to the peptide mixture and incubated for 1 h at room temperature. The results showed that with the first round of IMAC enrichment (IMAC-1), a total of 4661 peptides were identified from 3 mg of cell lysate within a 180 min LC-MS/MS run (with a 150 min gradient), and among these peptides, 3699 were phosphopeptides, with a phosphopeptide enrichment ratio of 79.4% (Supporting Information Table S3, Figure 3A). PhosphoRS was used to evaluate the accuracy of phosphosites localization.<sup>28</sup> As reported previously, phosphopeptides with PhosphoRS score  $\geq 99\%$  are considered to have confident phosphosite localization.<sup>28</sup> We only counted phosphopeptides with confident localization for mono- or multiphosphopeptide identification, as well as for calculating total number of phosphosites identified in all species. IMAC-1 enrichment generated 2608 phosphopeptides with confident localization information, among which 2166 were monophosphopeptides, while 442 were multiphosphopeptides (Supporting Information Table S3, Figure 3B).

To evaluate how complete a single IMAC enrichment is at extracting phosphopeptides from the whole cell lysate, we then carried out a second round of IMAC enrichment (IMAC-2) from the flow-through of IMAC-1. We repeated the process for

a third round (IMAC-3), with IMAC enrichment from the flow-through of IMAC-2. In IMAC-2 enrichment, 3079 total phosphopeptides were identified. Of these, 1791 phosphopeptides were also identified with IMAC-1, while 1288 phosphopeptides were unique to IMAC-2. With IMAC-3 enrichment, a total number of 1531 phosphopeptides were identified, among which 947 phosphopeptides that had been identified with IMAC-1 enrichment and 1252 phosphopeptides that overlapped with IMAC-2 enrichment. Only an additional 223 unique phosphopeptides were detected with IMAC-3 enrichment (Figure 3C), indicating that three cycles of IMAC enrichment would be enough to enrich most of the phosphopeptides from the whole cell lysates.

The multistep IMAC enrichment increased the number of identified phosphopeptides from 3699 unique phosphopeptides with a single IMAC enrichment to 4727 unique phosphopeptides (Supporting Information Table S5), an increased ratio of 27.8%. In addition, in each enrichment cycle, the distribution of enriched phosphopeptides was different. Most of the multiply phosphorylated peptides, a total of 442, were enriched in the first round of IMAC enrichment. In the second round of IMAC enrichment, only 9 multiply phosphorylated phosphopeptides were detected each containing 2 phosphate groups, while in the third round of IMAC enrichment, all identified phosphopep-

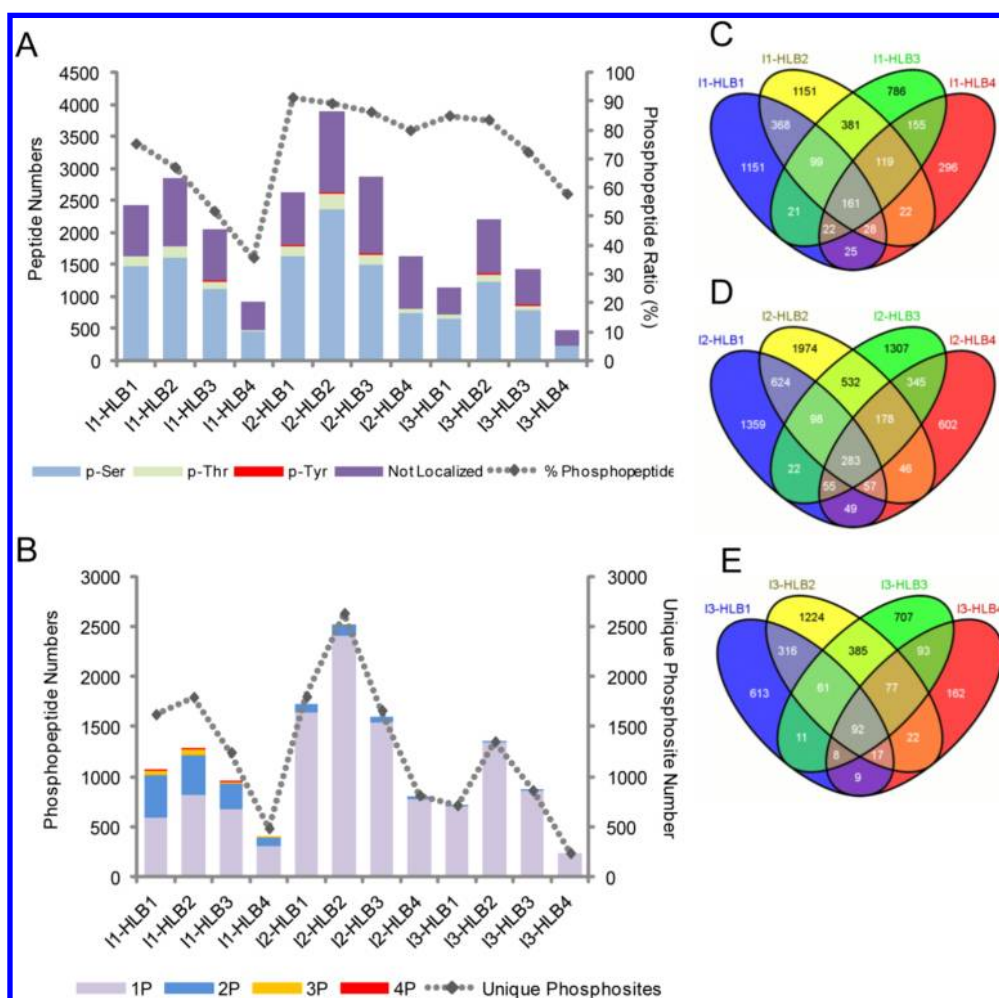


**Figure 4.** Distribution of phosphopeptides identified by the multi-IMAC-HLB method. (A) Number of identified phosphopeptides in each HLB fraction with phospho-serine (blue), phospho-threonine (green), or phospho-tyrosine (red) sites, and those without confident localization (phosphoRS score <99%, dark purple) are shown in the bar graph. Percentages of identified phosphopeptides from the total number of identified peptides in each HLB fraction are shown with the dashed line. (B) Numbers of identified phosphopeptides (phosphoRS score ≥99%) in each HLB fraction with 1, 2, 3, or 4 phosphate groups are shown in purple, blue, yellow and red colors. Unique phosphosite numbers in each HLB fraction are calculated from phosphopeptides with phosphoRS score ≥99% and are shown with the dashed line. (C, D, E) Overlap of the nonredundant phosphopeptides identified in each HLB fraction of the first (C), second (D), and third (E) round of IMAC enrichment are shown in the Venn diagram.

tides were singly phosphorylated (Figure 3B, Supporting Information Table S3). However, the distribution of p-Ser, p-Thr, and p-Tyr phosphosites, and the distribution of charge states of identified phosphopeptides did not vary among the three enrichment cycles (Figure 3A,D, Supporting Information Table S3).

#### Further Fractionation of Multistep IMAC Enrichment Fractions with High-pH HLB (Multi-IMAC-HLB) Increases Phosphopeptide Identification

Since the multistep IMAC enrichment method generates only 3 fractions, it might not be a suitable method for in-depth phosphopeptide identification. To maximize the number of phosphopeptides identified, we added another fractionation method after the IMAC enrichment steps to further simplify the samples. In addition, the IMAC process introduces salt to the samples so a desalting step is required before LC-MS/MS analysis. In order to reduce the number of manipulation steps and to decrease sample loss, we added a second dimension separation while desalting. We chose high-pH reverse phase separation as our second dimension method. Because the

normal RP packing materials cannot sustain a pH as high as 10, we used HLB cartridges that work similarly to reverse phase cartridges but are more suitable and efficient for peptide purification, and are stable under high pH. Phosphopeptides from each cycle of the multistep IMAC enrichment were applied to the HLB cartridges separately. Salt was removed by washing, and the peptides were eluted from the cartridge stepwise with increasing acetonitrile concentrations under high pH conditions. In order to decrease the instability of the phosphopeptides, the collection tubes were filled with 25  $\mu$ L of formic acid in advance, so that the eluted phosphopeptides would be protonated immediately after elution. It is reported that high pH LC chromatograms have complementary characteristics to low pH chromatography.<sup>25</sup> While typically the LC solvents are acidic, the high pH for the second dimension separation is expected to provide good orthogonality for the LC-MS/MS analysis. In order to decrease LC-MS/MS run time, we mixed the HLB fractions eluted with 5 and 25% ACN, 10 and 30% ACN, 15 and 35% ACN, and 20 and 80%



**Table 1. Summary of Phosphopeptides Identified with SCX-IMAC, Multi-IMAC, or Multi-IMAC-HLB Methods, and Comparison of the Efficiency of These Different Workflows**

workflow	total phosphopeptides	nonredundant phosphopeptides	p-Ser	p-Thr	p-Tyr	starting material (mg)	sample preparation time (day)	LC–MS/MS time (h) <sup>a</sup>	phosphopeptides identified per LC–MS/MS hour
SCX-IMAC	7907	5519	4658	306	25	15	7	44	125
Multi-IMAC	8309	4727	3350	309	26	3	3	18	263
Multi-IMAC-HLB	22785	8969	5655	626	55	3	4	40	224

<sup>a</sup>Time required for duplicate LC–MS/MS runs for each sample.

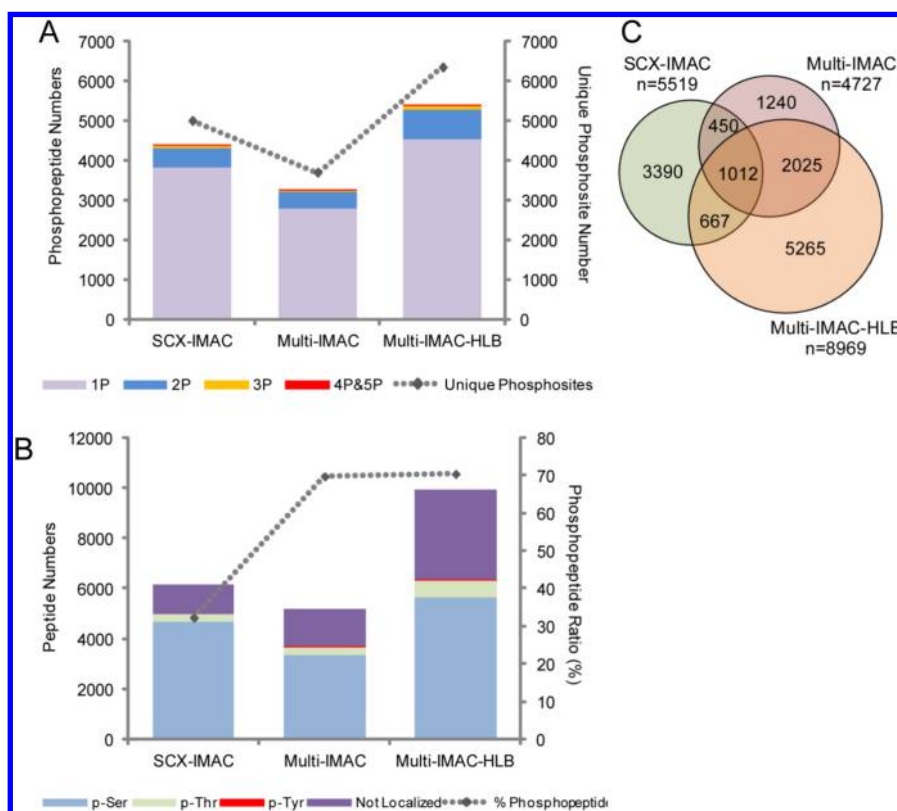


**Figure 5.** Comparison of phosphopeptide identifications from the SCX-IMAC, multistep IMAC, and multi-IMAC-HLB methods. (A) Numbers of identified phosphopeptides in each method with phosphoRS score  $\geq 99\%$  are shown in the bar graph. Phosphopeptides (phosphoRS score  $\geq 99\%$ ) with 1, 2, 3, or 4 and 5 phosphate groups are shown in purple, blue, yellow and red colors. Unique phosphosite numbers confirmed in each method are calculated from phosphopeptides with phosphoRS score  $\geq 99\%$  and are shown with the dashed line. (B) Numbers of phosphopeptides with phospho-serine (blue), phospho-threonine (green), or phospho-tyrosine (red) sites, and those without confident localization (phosphoRS score  $< 99\%$ , dark purple) are shown in the bar graph. Percentages of identified phosphopeptides from the total identified peptides from each method are shown with the dashed line. (C) Overlap of nonredundant phosphopeptides identified in each method are shown in the Venn diagram.

ACN, generating 4 HLB fractions for each IMAC enrichment cycle.

The multi-IMAC-HLB method generated 12 total fractions, and each of these fractions were analyzed by LC–MS/MS for a 100 min run with 73 min gradient of 3–30% ACN, the same LC–MS conditions as the SCX-IMAC method. The results showed that with the additional HLB fractionation, the total number of identified phosphopeptides increased to 8969 as compared to the 4727 phosphopeptides from the SCX-IMAC analysis (Supporting Information Table S5). The number of phosphopeptides with confident phosphosite localization increased from 3225 to 5328, while the total identified phosphosites also increased from 3686 to 6337 (Supporting Information Table S5), nearly twice as much as without HLB fractionation. Most of the IMAC-HLB fractions showed a

relatively high phosphopeptide ratio, around 70–80%, with a maximum of 91.2% (Supporting Information Table S4, Figure 4A). As shown in Figure 3B, most multiply phosphorylated peptides were detected following the first cycle of IMAC enrichment, while with the second and third rounds of IMAC enrichments, only a total number of 9 multiply phosphorylated peptides (with 2 phosphates) were identified. However, with HLB fractionation, the proportion of multiply phosphorylated peptides from IMAC-2 and IMAC-3 enrichment was increased (Supporting Information Table S4, Figure 4B). This fact indicates that in IMAC-2 and IMAC-3 enrichment, there are still multiply phosphorylated peptides that can be enriched, and that the lack of detection is largely limited by the complexity of the sample. Careful further fractionation could help to improve the identification of these multiply phosphorylated peptides.

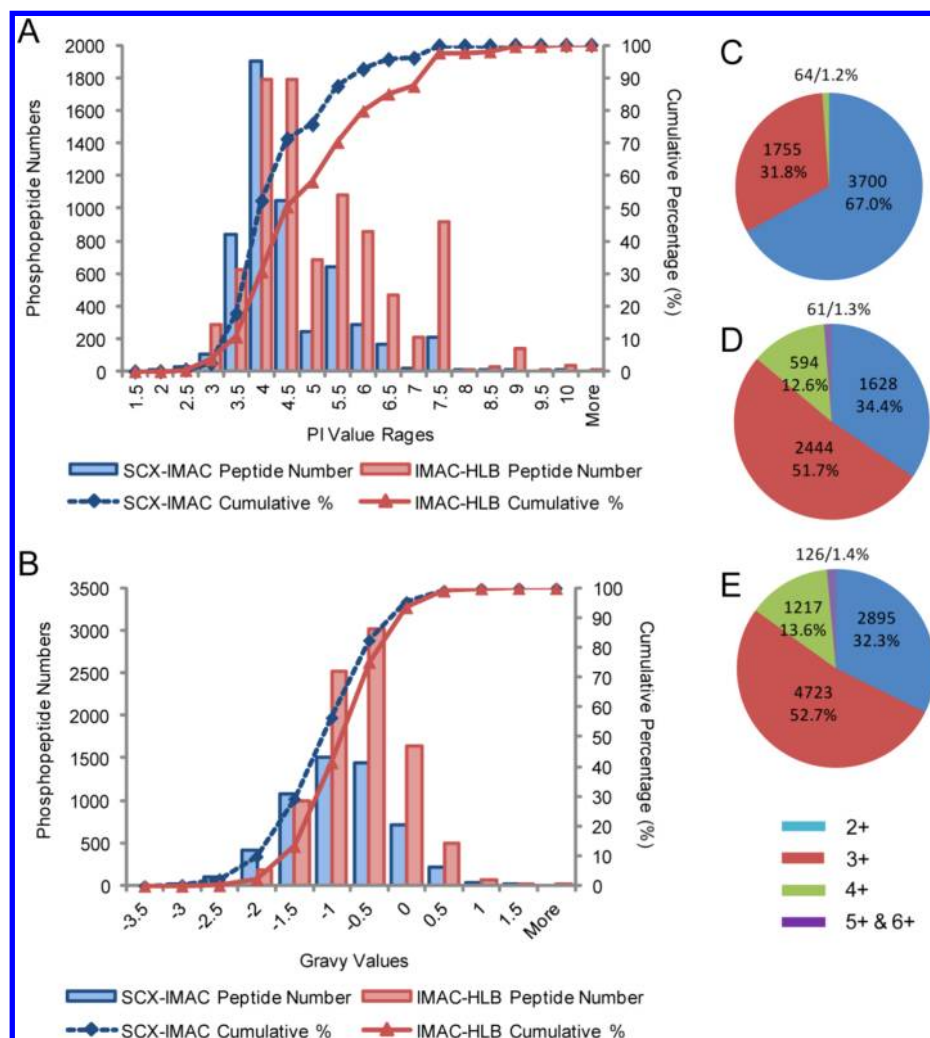


**Figure 6.** Comparison of phosphopeptide characteristics identified by the SCX-IMAC or multi-IMAC-HLB method. (A) Histogram of identified phosphopeptides with different pI value ranges by the SCX-IMAC (blue) or multi-IMAC-HLB (pink) method are shown in the bar graph. Cumulative percentage of phosphopeptides from low to high pI value ranges are shown with the dashed lines. (B) Histogram of identified phosphopeptides with different GRAVY value ranges by SCX-IMAC (blue) or multi-IMAC-HLB (pink) method are shown in bar graph. Cumulative percentage of phosphopeptides from low to high GRAVY value ranges are shown with the dashed lines. (C, D, E) Charge states of phosphopeptides identified in SCX-IMAC (C), multistep IMAC (D), and multi-IMAC-HLB (E) methods are shown in the pie chart.

The percentage of modified p-Ser, p-Thr, and p-Tyr did not show significant differences among the 12 IMAC-HLB fractions (Supporting Information Table S4, Figure 4A). The fractionation efficiency of HLB is shown in Figure 4C–E. We detected unique phosphopeptides in every HLB sample, indicating good efficiency of HLB fractionation.

#### Multi-IMAC-HLB Method Provides Higher Numbers of Identified Phosphopeptides, Using Less Starting Material, than the SCX-IMAC Method

We compared the number of phosphopeptides identified with SCX-IMAC method, the multistep IMAC enrichment, and the multi-IMAC-HLB method (Table 1). The multistep IMAC enrichment and multi-IMAC-HLB method require 3 mg of starting material, much less than the 15 mg needed for SCX-IMAC method. However, the number of identified phosphopeptides is greater with the multi-IMAC-HLB method, with 5519 phosphopeptides identified with SCX-IMAC compared to 8969 phosphopeptides identified with the multi-IMAC-HLB method (Supporting Information Table S5, Figure 5A). The increase in the numbers of identified phosphopeptides is not

because of the increase in the overall identified peptides (17060 with SCX-IMAC method and 12718 with multi-IMAC-HLB method) but is due to the increase in the ratio of identified phosphopeptides out of all detected peptides. The phosphopeptide ratio increased from 32.4% with SCX-IMAC method to 70.5% with multi-IMAC-HLB method (Supporting Information Table S5, Figure 5B). This difference can be attributed to the optimized IMAC conditions in multi-IMAC-HLB method. The ratio of p-Thr and p-Tyr residues was also increased with the multi-IMAC-HLB method as well as the multiply phosphorylated peptide percentage.

The overlap of these 3 methods showed that most of the phosphopeptides (64.2%) identified in multistep IMAC enrichment were also identified with the multi-IMAC-HLB method, although some phosphopeptides were lost during the treatment process (Figure 5C). The SCX-IMAC method has only 38.6% overlap with the multistep IMAC and multi-IMAC-HLB methods, indicating that SCX and HLB fractionation might have different characteristics and they might identify different populations of phosphopeptides.

### SCX-IMAC and Multi-IMAC-HLB Methods Identify Different Populations of Phosphopeptides

Because SCX and HLB separate peptides by dissimilar chemical principals and at different pH values, we compared the characteristics of phosphopeptides identified with these two distinct fractionation methods. The results show that with the SCX fractionation method, most of the identified phosphopeptides are acidic phosphopeptides with low *pI* values. The highest portion of phosphopeptides, 1906 in total, has *pI* values ranging from 3.5 to 4 (Figure 6A, Table 2A). For

**Table 2. Comparison of *pI* Value and GRAVY Ranges for Phosphopeptides Identified with SCX-IMAC or Multi-IMAC-HLB Method**

(A) Distribution of phosphopeptides of different <i>pI</i> value ranges identified by SCX-IMAC or Multi-IMAC-HLB method.				
<i>pI</i> values	SCX-IMAC		Multi-IMAC-HLB	
	phosphopeptide (#)	cumulative (%)	phosphopeptide (#)	cumulative (%)
1.5	0	0.0	0	0.0
2	2	0.0	0	0.0
2.5	29	0.6	32	0.4
3	109	2.5	292	3.6
3.5	840	17.8	622	10.6
4	1906	52.3	1791	30.5
4.5	1044	71.2	1787	50.5
5	247	75.7	681	58.1
5.5	645	87.4	1084	70.2
6	289	92.6	859	79.8
6.5	165	95.6	470	85.0
7	23	96.0	210	87.3
7.5	209	99.8	916	97.6
8	1	99.8	7	97.6
8.5	1	99.8	28	97.9
9	8	100.0	142	99.5
9.5	0	100.0	4	99.6
10	1	100.0	35	100.0
more	0	100.0	3	100.0

(B) Distribution of phosphopeptides of different GRAVY ranges identified by SCX-IMAC or Multi-IMAC-HLB method.				
GRAVY	SCX-IMAC		Multi-IMAC-HLB	
	phosphopeptide (#)	cumulative (%)	phosphopeptide (#)	cumulative (%)
−3.5	0	0.0	0	0.0
−3	21	0.4	0	0.0
−2.5	106	2.3	17	0.2
−2	417	9.9	182	2.2
−1.5	1070	29.2	997	13.3
−1	1505	56.5	2526	41.5
−0.5	1434	82.5	3024	75.2
0	710	95.4	1642	93.5
0.5	212	99.2	500	99.1
1	39	99.9	71	99.9
1.5	5	100.0	9	100.0
more	0	100.0	1	100.0

phosphopeptides with *pI* values lower than 4, 2886 phosphopeptides were identified with SCX-IMAC method, while 2737 phosphopeptides were identified with the multi-IMAC-HLB method, showing no difference between these two methods. However, the phosphopeptides with *pI* values higher than 4 increased from 2633 (47.7% of total) with the SCX-

IMAC method to 6232 (69.5% of total) with the multi-IMAC-HLB method (Table 2A). For the basic phosphopeptides with *pI* values higher than 7, only 220 (4.0% of total) phosphopeptides were identified with SCX-IMAC method, while this number increased to 1135 (12.7% of total) with the multi-IMAC-HLB method, a more than 5 times increase (Table 2A). The multi-IMAC-HLB method even identified 184 phosphopeptides with *pI* values higher than 8.5, while the SCX-IMAC method only identified 9. The dramatic increase in identifications for phosphopeptides with higher *pI* values likely results from the decrease of high *pI* peptide loss when performing the high-pH HLB separation. With the SCX method, under low pH, phosphopeptides with higher *pI* values are likely to be protonated, thus having a higher affinity to SCX resin. In order to elute these phosphopeptides, higher salt concentrations are required. However, high concentrations of salt make it difficult to solubilize the peptides. As a result, phosphopeptides with high *pI* values are difficult to recover from the SCX column and are readily lost during the SCX process. By contrast, with the high-pH HLB separation, there are no such problems, and these phosphopeptides can be more efficiently recovered.

The GRAVY values also showed differences between the two methods. With the SCX-IMAC method, 544 (9.9% of total) phosphopeptides were identified with GRAVY values lower than −2, while with the multi-IMAC-HLB method only 199 (2.2% of total) were identified (Figure 6B, Table 2B). However, for phosphopeptides with GRAVY values higher than −1.5, the multi-IMAC-HLB method showed a dramatic advantage and increased the phosphopeptide number from 3905 (70.8% of total) to 7773 (86.7% of total) (Table 2B). The reason for these differences would be due to the fact that SCX fractionates phosphopeptides mainly by their charge states, and the separation is performed under hydrophilic conditions, so that less hydrophilic phosphopeptides would be lost in the flow through during the separation. By comparison, HLB separates phosphopeptides mainly by their hydrophobicity with increasing acetonitrile percentage. Phosphopeptides with higher hydrophobicity are separated from the hydrophilic ones; thus, hydrophobic phosphopeptides have a greater chance to be fractionated and identified.

The charge states for the identified phosphopeptides were also substantially different between the SCX-IMAC and multi-IMAC-HLB data sets. In the SCX-IMAC method, 3700 phosphopeptides (67.0% of total) exist in the 2+ charge state, while in the multi-IMAC-HLB method only 2895 phosphopeptides (34.4% of total) were found at 2+ charge state. With the SCX-IMAC method, 1755 phosphopeptides (31.8% of total) were found at 3+ charge state, and this number increased to 4723 (52.7% of total) with the multi-IMAC-HLB method (Figure 6C-E, Supporting Information Table S5).

All the above-mentioned differences indicate that multi-IMAC-HLB and SCX-IMAC identify different populations of phosphopeptides. Because most of the fractionation methods used in phosphoproteomic studies are performed under very acidic conditions and separate phosphopeptides by hydrophilic interactions, the high-pH HLB fractionation method is complementary to other fractionation methods such as SCX, HILIC, or ERLIC to increase the overall phosphopeptide identification.



## CONCLUSION

In this study, we optimized the peptide-to-IMAC beads ratio for IMAC best performance. Three rounds of optimized IMAC enrichment were shown to be sufficient to enrich most of the phosphopeptides from whole cell mammalian lysates. Further fractionation with the high-pH HLB cartridges provided higher numbers of phosphopeptides and phosphosites and also increased the identified p-Thr and p-Tyr ratios, with significantly less starting material required compared to SCX-IMAC method. The multi-IMAC-HLB technique is relatively quick and easy to perform. Because the multi-IMAC-HLB method separates phosphopeptides in a high-pH range by differences in hydrophobicity, while most of the other fractionation methods perform at low-pH conditions, the multi-IMAC-HLB method shows dramatic improvement for identification of phosphopeptides with higher pI and GRAVY values. The charge states of identified phosphopeptides with SCX-IMAC or multi-IMAC-HLB method are also significantly different. SCX-IMAC mostly enriched phosphopeptides with a 2+ charge state, while multi-IMAC-HLB preferentially enriched phosphopeptides with a 3+ charge state. In conclusion, multi-IMAC-HLB method is a relatively easy and efficient approach to enrich for phosphopeptides, especially basic and hydrophobic phosphopeptides, from less starting material than is required by other commonly used approaches.

## ASSOCIATED CONTENT

### Supporting Information

Supporting tables and figures. These materials are available free of charge via the Internet at <http://pubs.acs.org>.

## AUTHOR INFORMATION

### Corresponding Author

\*(A.B.H.) Tel.: 574-631-0583. Fax: 574-631-6652. E-mail: [ahummon@nd.edu](mailto:ahummon@nd.edu).

### Notes

The authors declare no competing financial interest.

## ACKNOWLEDGMENTS

The work was funded by Walther Cancer Foundation and the Notre Dame Harper Cancer Research Institute for postdoctoral funding for X.S.Y. The work was also funded by Department of Defense Visionary Postdoctoral Fellowship Award to X.S.Y. (USAMRAA W81XWH-12-1-0412). We thank the staff from the Mass Spectrometry and Proteomics Facility at the University of Notre Dame, especially Dr. Bill Boggess, for their helpful discussions and advice, and for their help maintaining the mass spectrometry equipment. We thank Dr. Susan Skube for her revisions and advice on this manuscript.

## REFERENCES

- (1) Harsha, H. C.; Pandey, A. Phosphoproteomics in cancer. *Mol. Oncol.* **2010**, *4* (6), 482–95.
- (2) Iliuk, A.; Liu, X. S.; Xue, L.; Liu, X.; Tao, W. A. Chemical visualization of phosphoproteomes on membrane. *Mol. Cell. Proteomics* **2012**, *11* (9), 629–39.
- (3) Wei, X.; Li, L. Mass spectrometry-based proteomics and peptidomics for biomarker discovery in neurodegenerative diseases. *Int. J. Clin. Exp. Pathol.* **2009**, *2* (2), 132–48.
- (4) Iliuk, A. B.; Tao, W. A. Is phosphoproteomics ready for clinical research? *Clin. Chim. Acta* **2013**, *420*, 23–7.
- (5) Andersson, L.; Porath, J. Isolation of phosphoproteins by immobilized metal ( $\text{Fe}^{3+}$ ) affinity chromatography. *Anal. Biochem.* **1986**, *154* (1), 250–4.
- (6) Iliuk, A. B.; Martin, V. A.; Alicie, B. M.; Geahlen, R. L.; Tao, W. A. In-depth analyses of kinase-dependent tyrosine phosphoproteomes based on metal ion-functionalized soluble nanopolymers. *Mol. Cell. Proteomics* **2010**, *9* (10), 2162–72.
- (7) Ikeguchi, Y.; Nakamura, H. Determination of organic phosphates by column-switching high performance anion-exchange chromatography using on-line preconcentration on titania. *Anal. Sci.* **1997**, *13* (3), 479–85.
- (8) Wang, W. H.; Palumbo, A. M.; Tan, Y. J.; Reid, G. E.; Tepe, J. J.; Bruening, M. L. Identification of p65-associated phosphoproteins by mass spectrometry after on-plate phosphopeptide enrichment using polymer-oxotitanium films. *J. Proteome Res.* **2010**, *9* (6), 3005–15.
- (9) Peng, J.; Elias, J. E.; Thoreen, C. C.; Licklider, L. J.; Gygi, S. P. Evaluation of multidimensional chromatography coupled with tandem mass spectrometry (LC/LC–MS/MS) for large-scale protein analysis: the yeast proteome. *J. Proteome Res.* **2003**, *2* (1), 43–50.
- (10) Han, G.; Ye, M.; Zhou, H.; Jiang, X.; Feng, S.; Jiang, X.; Tian, R.; Wan, D.; Zou, H.; Gu, J. Large-scale phosphoproteome analysis of human liver tissue by enrichment and fractionation of phosphopeptides with strong anion exchange chromatography. *Proteomics* **2008**, *8* (7), 1346–61.
- (11) Zarei, M.; Sprenger, A.; Gretzmeier, C.; Dengjel, J. Combinatorial use of electrostatic repulsion-hydrophilic interaction chromatography (ERLIC) and strong cation exchange (SCX) chromatography for in-depth phosphoproteome analysis. *J. Proteome Res.* **2012**, *11* (8), 4269–76.
- (12) McNulty, D. E.; Annan, R. S. Hydrophilic interaction chromatography reduces the complexity of the phosphoproteome and improves global phosphopeptide isolation and detection. *Mol. Cell. Proteomics* **2008**, *7* (5), 971–80.
- (13) Gan, C. S.; Guo, T.; Zhang, H.; Lim, S. K.; Sze, S. K. A comparative study of electrostatic repulsion-hydrophilic interaction chromatography (ERLIC) versus SCX-IMAC-based methods for phosphopeptide isolation/enrichment. *J. Proteome Res.* **2008**, *7* (11), 4869–77.
- (14) Zarei, M.; Sprenger, A.; Metzger, F.; Gretzmeier, C.; Dengjel, J. Comparison of ERLIC-TiO<sub>2</sub>, HILIC-TiO<sub>2</sub>, and SCX-TiO<sub>2</sub> for global phosphoproteomics approaches. *J. Proteome Res.* **2011**, *10* (8), 3474–83.
- (15) Hennrich, M. L.; Groenewold, V.; Kops, G. J.; Heck, A. J.; Mohammed, S. Improving depth in phosphoproteomics by using a strong cation exchange-weak anion exchange-reversed phase multidimensional separation approach. *Anal. Chem.* **2011**, *83* (18), 7137–43.
- (16) Engholm-Keller, K.; Hansen, T. A.; Palmisano, G.; Larsen, M. R. Multidimensional strategy for sensitive phosphoproteomics incorporating protein prefractionation combined with SIMAC, HILIC, and TiO<sub>2</sub> chromatography applied to proximal EGF signaling. *J. Proteome Res.* **2011**, *10* (12), 5383–97.
- (17) Kettenbach, A. N.; Gerber, S. A. Rapid and reproducible single-stage phosphopeptide enrichment of complex peptide mixtures: application to general and phosphotyrosine-specific phosphoproteomics experiments. *Anal. Chem.* **2011**, *83* (20), 7635–44.
- (18) Villen, J.; Gygi, S. P. The SCX/IMAC enrichment approach for global phosphorylation analysis by mass spectrometry. *Nat. Protoc.* **2008**, *3* (10), 1630–8.
- (19) Zhai, B.; Villen, J.; Beausoleil, S. A.; Mintseris, J.; Gygi, S. P. Phosphoproteome analysis of *Drosophila melanogaster* embryos. *J. Proteome Res.* **2008**, *7* (4), 1675–82.
- (20) Treeck, M.; Sanders, J. L.; Elias, J. E.; Boothroyd, J. C. The phosphoproteomes of *Plasmodium falciparum* and *Toxoplasma gondii* reveal unusual adaptations within and beyond the parasites' boundaries. *Cell Host Microbe* **2011**, *10* (4), 410–9.
- (21) Stone, M. D.; Chen, X.; McGowan, T.; Bandhakavi, S.; Cheng, B.; Rhodus, N. L.; Griffin, T. J. Large-scale phosphoproteomics

analysis of whole saliva reveals a distinct phosphorylation pattern. *J. Proteome Res.* **2011**, *10* (4), 1728–36.

(22) Wang, Y.; Yang, F.; Gritsenko, M. A.; Wang, Y.; Clauss, T.; Liu, T.; Shen, Y.; Monroe, M. E.; Lopez-Ferrer, D.; Reno, T.; Moore, R. J.; Klemke, R. L.; Camp, D. G. Nd.; Smith, R. D. Reversed-phase chromatography with multiple fraction concatenation strategy for proteome profiling of human MCF10A cells. *Proteomics* **2011**, *11* (10), 2619–26.

(23) Siu, S. O.; Lam, M. P.; Lau, E.; Kong, R. P.; Lee, S. M.; Chu, I. K. Fully automatable two-dimensional reversed-phase capillary liquid chromatography with online tandem mass spectrometry for shotgun proteomics. *Proteomics* **2011**, *11* (11), 2308–19.

(24) Yang, F.; Shen, Y.; Camp, D. N.; Smith, R. D. High-pH reversed-phase chromatography with fraction concatenation for 2D proteomic analysis. *Expert Rev. Proteomics* **2012**, *9* (2), 129–34.

(25) Song, C.; Ye, M.; Han, G.; Jiang, X.; Wang, F.; Yu, Z.; Chen, R.; Zou, H. Reversed-phase-reversed-phase liquid chromatography approach with high orthogonality for multidimensional separation of phosphopeptides. *Anal. Chem.* **2010**, *82* (1), 53–6.

(26) Gauci, S.; van Breukelen, B.; Lemeer, S. M.; Krijgsveld, J.; Heck, A. J. A versatile peptide pI calculator for phosphorylated and N-terminal acetylated peptides experimentally tested using peptide isoelectric focusing. *Proteomics* **2008**, *8* (23–24), 4898–906.

(27) Li, Q. R.; Ning, Z. B.; Tang, J. S.; Nie, S.; Zeng, R. Effect of peptide-to-TiO<sub>2</sub> beads ratio on phosphopeptide enrichment selectivity. *J. Proteome Res.* **2009**, *8* (11), 5375–81.

(28) Taus, T.; Kocher, T.; Pichler, P.; Paschke, C.; Schmidt, A.; Henrich, C.; Mechtler, K. Universal and confident phosphorylation site localization using phosphoRS. *J. Proteome Res.* **2011**, *10* (12), 5354–62.